Evaluating MJO Event Initiation and Decay in the Skeleton Model using an RMM-like Index

Justin P. Stachnik[*1,2], Duane E. Waliser[1, 2], Andrew J. Majda[3], Samuel N. Stechmann[4], and Sulian Thual[3]

1. Joint Institute for Regional Earth System Science and Engineering, University of California, Los Angeles, Los Angeles, CA, USA.

2. Jet Propulsion Laboratory, California Institute of Technology, Pasadena, CA, USA.

3. Department of Mathematics and Center for Atmosphere–Ocean Science, Courant Institute, New York University, New York, NY, USA.

4. Department of Mathematics and Department of Atmospheric and Oceanic Sciences, University of Wisconsin–Madison, Madison, WI, USA.

Submitted 9 July 2015

to Journal of Geophysical Research-Atmospheres

[*] Corresponding author: Justin P. Stachnik, Jet Propulsion Laboratory, 4800 Oak Grove Drive, M/S 233-304, Pasadena, CA 91109, USA. (Justin.P.Stachnik@jpl.nasa.gov)

Key Points

- An RMM-like index was created for the skeleton model that mimics observations
- Stochasticity helps improve MJO initiation and termination event statistics
- The skeleton model produces more realistic MJOs when forced with observed SSTs

Abstract

The Madden-Julian oscillation (MJO) skeleton model is a low-order dynamic model that is capable of simulating many of the observed features of the MJO. This study develops a model-based "MJO" index that is similar to the well-known real-time multivariate MJO (RMM) index to better facilitate comparison between the skeleton model and observational data. Multivariate and univariate empirical orthogonal function (EOF) analyses were performed on the convective heating and zonal wind data taken from the skeleton model for simulations forced with an idealized warm pool and observed sea surface temperatures (SSTs). The leading EOF modes indicated a wavenumber-1 convectively-coupled circulation anomaly with zonal asymmetries that closely resembled the observed RMM EOFs, especially when the model was forced with observed SSTs. The RMM-like index was used to compute an MJO climatology and document the occurrence of primary, continuing, and terminating MJO events in the skeleton model. The overall amount of MJO activity and event lengths compared reasonably well to observations for such a simple model. Attempts at reconciling the observed geographic distribution of MJO events were not successful for the stochastic simulations, though stochasticity is necessary in order to produce composite MJOs that initiate and decay with time scales similar to observations. Finally, analysis indicates that the existence of higher-frequency, eastward travelling waves with higher wavenumbers ($k \approx 12$) embedded within the large-scale flow often precedes MJO termination in the skeleton model.

1. Introduction

Intraseasonal variability of the tropical atmosphere is dominated by an eastward propagating equatorial mode known as the Madden-Julian oscillation (MJO), appropriately named after its initial discoverers [*Madden and Julian*, 1971; 1972]. The MJO represents a convectively-coupled mode of cloud and circulation anomalies with planetary scale (i.e., generally at wavenumbers 1-3) and an oscillation frequency of roughly 30-60 days [*Madden and Julian*, 1994; *Zhang*, 2005]. Deep convection associated with an MJO event generally appears as a broad envelope of cloud and precipitation anomalies that most commonly begins over the western or central Indian Ocean [e.g., *Matthews*, 2008; *Straub*, 2013] and propagates eastward at ~5 m s^{-1} until eventually terminating over the maritime continent or the central Pacific [e.g., *Stachnik et al.*, 2015]. The MJO directly impacts local weather and tropical climate and has also been shown to have far reaching dynamical effects including modifying the global monsoons [*Lau and Chan*, 1986; *Goswami and Ajaya Mohan*, 2001; *Matthews*, 2004; *Wheeler and Hendon*, 2004], genesis and intensification of tropical cyclones [*Maloney and Hartmann*, 2000; *Jiang et al.*, 2012], mid-latitude weather anomalies [*Higgins et al.*, 2000; *Bond and Vecchi*, 2003; *Guan et al.*, 2012], and may impact the onset of El Niño-Southern Oscillation (ENSO) events [e.g., *Lau and Waliser*, 2005].

Despite its global importance, successfully simulating the MJO remains a challenge in most global climate and weather forecast models [e.g., *Slingo et al.*, 1996, *Waliser et al.*, 1999, *Zhang et al.*, 2006; *Hung et al.*, 2013; *Jiang et al.*, 2015]. Global climate models (GCMs) generally struggle with initiating MJO events and often simulate weaker eastward propagation than observed in nature. Models with more realistic MJOs usually tune specific model parameters including estimates of air-sea coupling, the sensitivity of parameterized convection to

atmospheric moisture, or increase deep convection entrainment rates in order to delay convection (among others), which often comes at the sacrifice of a larger bias in the mean state [e.g., *Bechtold et al.*, 2008; *Hannah and Maloney*, 2011; *Benedict et al.*, 2013; *Klingaman and Woolnough*, 2014a; *Klingaman and Woolnough*, 2014b]. Recent advances using superparameterizations, in which a cloud resolving model is embedded within each GCM gridpoint, have demonstrated some success at improving simulations of the MJO [e.g., *Grabowski*, 2003; *Benedict and Randall*, 2009; *Pritchard and Bretherton*, 2014]. Nevertheless, these enhancements are inherently linked to a significant increase in the computational expense. Simple theoretical models, such as the multicloud model of *Khouider and Majda* [2006, 2007], have also been shown to improve simulated MJO variability when incorporated into aquaplanet and coarse-resolution GCMs [*Khouider et al.*, 2011; *Ajayamohan et al.*, 2013; *Deng et al.*, 2015]. Regardless, there is a pressing need for the refined development of computationally inexpensive, low-order models that are fully capable of simulating the large-scale, observed features of the MJO. Furthermore, incorporating these fundamental MJO dynamics into higher-order models may also help improve intraseasonal and medium-range weather forecasts.

The MJO skeleton model, developed by *Majda and Stechmann* [2009, 2011], is one such example of a low-order dynamical model that successfully simulates a number of salient features of the MJO including (1) an eastward propagation at ~5 m s^{-1}, (2) a unique dispersion relation with $\partial\omega/\partial k \approx 0$, and (3) a horizontal quadrupole vortex structure. Recent work by *Thual et al.* [2014] incorporated a stochastic element into the convective parameterization of the skeleton model and was able to further simulate (4) observed MJO event intermittency and (5) the organization of MJOs into circumnavigating events and wave trains as seen in nature [e.g., *Matthews*, 2008; *Yoneyama et al.*, 2013]. These MJO-like waves have also been positively

identified in observational data by *Stechmann and Majda* [2015] and *Ogrosky and Stechmann* [2015] using a new index that projects reanalysis data onto the theoretical linear solutions of the MJO obtained from the skeleton model (i.e., the amplitudes of the Kelvin and equatorial Rossby wave structures, moisture anomalies, and amplitude of convective heating). While the above index is proficient at isolating the observed MJO signal without the use of time filtering or empirical orthogonal functions (EOFs), its use should be supplemented by more common MJO metrics in order to better facilitate comparisons with higher-order GCMs and operational weather forecast models.

This work intends to evaluate and build a complementary index for the MJO skeleton model based on the widely-used real-time multivariate MJO (RMM) index of *Wheeler and Hendon* [2004]. The RMM index has experienced tremendous popularity over the last decade and there are a large number of studies that composite MJO data by RMM phase and permit a more direct comparison between the skeleton model and observations or GCMs. Moreover, defining an RMM-like index for the skeleton model provides the opportunity to evaluate higher-order features of the model solutions in a framework consistent with observations including MJO event climatology and the precursor conditions associated with the initiation and termination of MJO events.

This article is organized as follows. Section 2 gives a brief overview of the skeleton model in addition to the methods used to derive the RMM-like index. We extend the recent work by *Ogrosky and Stechmann* [2015] and run the model using either an idealized warm pool or a realistic background state calculated from observed sea surface temperatures (SSTs). Comparisons of the fundamental MJO structures in the model are evaluated in the RMM-like framework and presented in section 3. We also evaluate the overall level of MJO activity in the

113 model along with several applications that include a comparison to the observed MJO event
114 climatology and identification of precursor conditions potentially responsible for MJO
115 termination following *Stachnik et al.* [2015]. Finally, section 4 closes with a summary and
116 discussion of key results while identifying avenues for continued and potential future work.
117
118 **2. Data and Methods**
119 *2.1. The Skeleton Model*
120 The MJO skeleton model [*Majda and Stechmann*, 2009, 2011] is a low-order, nonlinear
121 oscillator designed to qualitatively reproduce the main features of tropical atmospheric dynamics
122 at intraseasonal time and planetary scales. The skeleton model is unique in that the large-scale
123 waves are assumed to arise through neutrally stable interactions involving convectively-coupled
124 waves at the synoptic and mesoscale that are driven by planetary scale moisture anomalies
125 instead of instabilities that occur on the planetary scale. Strictly speaking, the basic model
126 premise assumes that the instabilities and damping take place on the synoptic or mesoscale, the
127 details of which are unimportant for the resulting amplitude of the convective heating that drives
128 the large-scale circulation anomalies diagnosed at the planetary scale.
129 Consequently, the skeleton model comprises a simple Matsuno-Gill type model of the
130 equatorial primitive shallow water equations, without damping, to sufficiently represent the
131 planetary scale, dry dynamics (Equations 1-4). In addition, there are two evolution equations that
132 describe the time tendencies of the amplitude of the convective heating wave envelope and lower
133 tropospheric moisture anomalies, respectively (Equations 5-6). Given that observations of the
134 MJO often demonstrate positive low-level moisture anomalies preceding and in quadrature to
135 regions of deep convection [e.g., *Hendon and Salby*, 1994; *Myers and Waliser*, 2003], the

skeleton model parameterizes the time tendency of the convective envelope amplitude (a) as a function of lower tropospheric moisture anomalies (q). This relationship is signified by the nonlinear amplitude equation in the following set (Equation 7). The model equations in non-dimension units are thus

$$\frac{\partial u}{\partial t} - yv = -\frac{\partial p}{\partial x} \quad (1)$$

$$yu = -\frac{\partial p}{\partial y} \quad (2)$$

$$0 = -\frac{\partial p}{\partial z} + \theta \quad (3)$$

$$\frac{\partial u}{\partial x} + \frac{\partial v}{\partial y} + \frac{\partial w}{\partial z} = 0 \quad (4)$$

$$\frac{\partial \theta}{\partial t} + w = \bar{H}a - s^{\theta} \quad (5)$$

$$\frac{\partial q}{\partial t} - \bar{Q}w = -\bar{H}a + s^{q} \quad (6)$$

$$\frac{\partial a}{\partial t} = \Gamma q a, \quad (7)$$

where u, v, and w represent the zonal, meridional, and vertical velocities, respectively, p is pressure, and θ is potential temperature. $\bar{H}$ and $\bar{Q}$ are constants that scale the heating rate and approximate the background vertical moisture gradient, respectively. The quantity Γ is a positive proportionality constant. Finally, s^q and s^θ represent external radiative cooling and moistening terms that can be used to force the model. It should be noted that all variables, with the exception of a, are anomalies from a radiative-convective equilibrium state.

We use the simplest version of the skeleton model herein, where the above equations are reduced to a single dimension by horizontally and vertically truncating to retain only the first meridional Hermite function and vertical baroclinic mode. The effect of the meridional truncation is to maintain an equatorially symmetric heating structure that excites only Kelvin

waves and the first equatorially symmetric Rossby waves. Details of the truncations, along with the equations for the model solutions and their reconstructed variables, are provided in *Majda and Stechmann* [2009, 2011].

Recently, *Thual et al.* [2014] modified the nonlinear term qa in the convective parameterization (Equation 7) to include a stochastic birth-death process to better account for the effects of synoptic and mesoscale processes that introduce significant irregularity to the MJO. Specifically, the amplitude of the convective envelope was replaced by a random variable, a, that evolves according to

$$a = \Delta a \eta, \qquad (8)$$

where Δa is a fixed step and η is a non-negative integer. The probability (P) of any given value η is prescribed by the master equation

$$\frac{\partial P(\eta)}{\partial t} = [\lambda(\eta - 1)P(\eta - 1) - \lambda(\eta)P(\eta)] + [\mu(\eta + 1)P(\eta + 1) - \mu(\eta)P(\eta)], \qquad (9)$$

where λ and μ are the upward and downward transition rates, respectively. It should be noted that these transitions are small and the parameters have been carefully chosen such that the long-term average of the stochastic model solutions recovers the dynamics of the original deterministic model. Additional details regarding the stochastic version of the skeleton model are provided in *Thual et al.* [2014].

This study continues to apply the previous condition where the external sources of cooling and moistening are set equal (i.e., $s^q = s^\theta$), which conserves the vertically integrated moist static energy. This balance condition was used for both a horizontally homogeneous and idealized warm pool state in *Majda and Stechmann* [2009, 2011] and *Thual et al.* [2014], where the latter is shown by a simple cosine pattern in Figure 1a with its maximum amplitude shifted towards the longitudes where it is actually observed. Furthermore, the zonal average of the

external terms must be equal (i.e., $\overline{s^q} = \overline{s^\theta}$) in order for a steady-state solution to exist without damping in the above model [e.g., *Majda and Klein*, 2003]. In the interest of producing the best possible comparison with the observed RMM index, we also perform several new simulations using the National Oceanic and Atmospheric Administration (NOAA) Optimum Interpolation (OI) version 2 (v2) SSTs [*Reynolds et al.*, 2002] in order to provide a more realistic estimate of the zonal variability of the external forcing terms used in the model simulations. While the above approach is far simpler than using observed estimates of diabatic heating, convective heating, and latent heat fluxes to force the skeleton model [*Ogrosky and Stechmann*, 2015], it is nevertheless a meaningful assumption that zonal variations in moisture anomalies, radiative cooling, and convection arise primarily from the distribution of SSTs, particularly for a long-term climatology as considered in this study.

The annual average NOAA OI SSTs v2 (1971-2000) were meridionally averaged from 10°S-10°N and regridded to match the relatively coarse horizontal resolution of the skeleton model (625 km). A Poisson relaxation was also performed to interpolate over missing data (i.e., land) and the resulting zonal profile was smoothed such that it only retains contributions from the first eight Fourier modes (Figure 1b). Overall, the observed SSTs closely match the shape of the idealized warm pool, especially over the Maritime Continent and Pacific Ocean (120°E-120°W). Most notably, there is a secondary maximum in the observed SSTs over the Atlantic Ocean (60°W-0°E) and a slightly weaker zonal gradient over the Indian Ocean (60°E-120°E) than otherwise present in the idealized warm pool case. The effect of these differences on the MJO-like waves in the skeleton model will be further explored in section 3.

2.2. Defining an RMM-like Index

As previously mentioned, *Stechmann and Majda* [2015] developed an MJO skeleton index that successfully identified the MJO in observational data by projecting reanalysis onto the MJO modes obtained from the skeleton model when using a uniform background state [i.e., $s^q(x) = s^\theta(x) = \overline{s}^\theta$]. Thus, rather than an empirical basis function like the RMM indices, this index is based on a theoretically based basis function obtained from the model. This analysis was extended in *Ogrosky and Stechmann* [2015] to a case with zonally varying forcing where $s^q(x) \neq s^\theta(x)$, which again summarizes the information from all MJO wavenumbers into a single index quantity. While the MJO skeleton index has several advantages including not requiring any time-filtering nor the use of EOF analysis, its potential for comparison to previous work is mostly limited due to the relative newness of this index combined with a change in the means of obtaining the basis function.

In the present work, we develop an MJO index for the skeleton model that mimics the methods of the RMM index from *Wheeler and Hendon* [2004]. Although there are many other indices that are currently used to identify the MJO including wavenumber-frequency filtering [e.g., *Wheeler et al.*, 2000], lower-tropospheric wind [e.g., *Maloney and Hartmann*, 1998], upper-troposphere divergence and velocity potential [e.g., *Chen and Del Genio*, 2009; *Ventrice et al.*, 2013], or time-filtered outgoing longwave radiation (OLR) and cloudiness datasets [e.g., *Hendon and Salby*, 1994; *Matthews*, 2000; *Matthews*, 2008; *Kiladis et al.*, 2014], the choice of the RMM index is particularly appropriate here given the fact that the RMM index is primarily sensitive to wavenumber-1 modes, planetary scale circulation anomalies, and a baroclinic structure [e.g., *Straub*, 2013] that are likely to be reproduced by the skeleton model given its focus on these scales.

225 The RMM is a combined index of cloudiness and circulation anomalies based on
226 observed OLR and lower- and upper-tropospheric zonal winds taken from reanalysis data.
227 Accordingly, we must first decide what model variables are most appropriate to use as
228 observational proxies when creating an RMM-like index from the skeleton model. The following
229 analysis uses the zonal wind from the skeleton model as a direct substitute for the lower-
230 tropospheric wind, whereas the convective (latent) heating variable $\overline{H}a$ is used as a proxy for the
231 observed OLR. *Stechmann and Ogrosky* [2014] showed that variations in the total diabatic
232 heating (i.e., $\overline{H}a - s^{\theta}$) were directly proportional to OLR in the tropics, especially when
233 averaged for long time periods (i.e., multiple years or decades) as done in our analysis. As such,
234 positive $\overline{H}a$ anomalies (enhanced heating) can thus be thought to have the same physical
235 interpretation as negative OLR anomalies (enhanced cloudiness and deep convection) in our
236 index.
237 Following *Wheeler and Hendon* [2004], daily anomalies of the skeleton model variables
238 were initially calculated by removing the long-term mean and first three harmonics of the annual
239 cycle. It should be noted that while *Wheeler and Hendon* [2004] considered global data between
240 15°S-15°N, the skeleton model analysis is restricted to data strictly at the equator since the initial
241 truncation only retains the first meridional mode (i.e., no asymmetric modes). *Wheeler and*
242 *Hendon* [2004] continue to remove longer-term variability by subtracting the component linearly
243 related to a measure of ENSO SSTs and further subtract a 120-day mean of the previous 120
244 days to remove any additional aspects of interannual or decadal variability and long-term trends.
245 Since the skeleton model does not account for ENSO physics and variability nor contains any
246 time-dependent SSTs (recall, s^q and s^{θ} are fixed), we choose to instead time filter the daily
247 anomalies using a 20-100 day Lanczos filter with 201 weights in order to isolate the

intraseasonal signal following *Matthews* [2008]. Each variable in the time-filtered dataset is normalized by its global variance to ensure equal contributions to the combined EOF analysis, again using the methods documented in *Wheeler and Hendon* [2004]. Both univariate and multivariate EOF analyses were performed on the convective heating and zonal wind data taken from the skeleton model simulations, with the leading two EOF modes used to calculate the model principal components. Finally, the principal components from each simulation and corresponding EOF analysis were normalized by their standard deviation such that a value of unity represents anomalies of one standard deviation from the mean.

We refer to the RMM-like index for the model simulations as the skeleton multivariate MJO index (SMM) as we only briefly consider those cases using a univariate analysis. Likewise, the principal components from the skeleton model data are termed SMM1 and SMM2 and are assigned their order based on which of the two leading EOFs most closely resembles the observed *Wheeler and Hendon* [2004] structures. The values of SMM1 and SMM2 can therefore be visualized in a 2-dimensional phase space similar to the RMM index with significant MJO activity defined as an SMM amplitude greater than or equal to one with eastward propagation indicated by a counter-clockwise rotation of the daily amplitudes in the phase space.

3. Results

The following analysis presents a comparison of the skeleton model simulations with either an idealized warm pool or the truncated, observed SSTs using the model set-up and framework established by *Thual et al.* [2014]. The default parameters and model constants for all simulations were also taken from *Thual et al.* [2014], with the sole exception that the zonal average of the radiative cooling term, $\overline{s^{\theta}(x)}$, is set equal to 1.0 K day^{-1} and 1.33 K day^{-1} for the

idealized warm pool and observed SST cases, respectively. Although the skeleton model has recently been amended to include a seasonally migrating warm pool and multiple meridional modes [*Thual et al.*, 2015], in addition to a refined vertical structure [*Thual and Majda*, 2015], we restrict our initial discussion to the stochastic and deterministic model simulations using the idealized and observed, annual average SSTs.

3.1. Climatology and Variance of Simulations using Idealized and Observed Forcing

Time-longitude series of the anomalous 10-100 day filtered skeleton model variables ($\overline{H}a$, u, and q) are shown in Figure 2 for a representative 600 day period for the simulations using the idealized warm pool and truncated, observed SSTs (Case-WP and Case-SST8N, respectively). In both cases, there appear to be several instances of eastward propagating, MJO-like waves that travel at approximately 5-6 m s^{-1} throughout the domain. These waves are evident throughout the entire period for Case-WP in the zonal wind (Figure 2b) with coherent eastward propagating structures not appearing until day 38200 for Case-SST8N (Figure 2e). Although specific MJO events should not be directly compared between the two simulations, Case-SST8N displays greater variance in the convective heating over the western Indian Ocean (i.e., 60-90°E) and a stronger mean convective heating over the tropical Atlantic (60°W-0°E) than identified for Case-WP (cf. Figures 2a and 2d). These areas of enhanced heating agree exceedingly well with *Ogrosky and Stechmann* [2015], who calculated observed $\overline{H}a$ values from precipitation data using the Global Precipitation Climatology Project (GPCP) [*Huffman et al.*, 2012] and similar model quantities from simulations forced with observed atmospheric OLR and latent heat fluxes derived from reanalysis data [Figure 13 in *Ogrosky and Stechmann*, 2015].

293 Power spectra of the reconstructed convective heating and zonal wind as a function of the
294 zonal wavenumber (k) and frequency (ω) are shown in Figure 3 for a 34 year period from each
295 model simulation. Both Case-WP and Case-SST8N demonstrate significant power in the MJO
296 range (i.e., $1 \leq k \leq 5$ and $1/90 \leq \omega \leq 1/30$ cpd) with the peak power stretching along a band with
297 $\partial\omega/\partial k \approx 0$, an auspicious and recurring feature of the skeleton model [*Thual et al.*, 2014]. The
298 peak power in each case is also near the dispersion curves of the linear solutions of the skeleton
299 model (the black circles in Figure 3). As in *Waliser et al.* [2009], the breadth of the peak in
300 frequency and wavenumber for the convective heating (i.e., a proxy for precipitation) relative to
301 zonal wind is captured by the skeleton model, though the convective heating power in the MJO
302 band is nearly constant with increasing wavenumber unlike in observations where the
303 precipitation power is largely confined to $1 \leq k \leq 3$. Generally, the convective heating and zonal
304 wind for Case-SST8N shows increased power near the dispersion curves of both the MJO and
305 moist Rossby modes, likely due to the slightly higher values of s^q and s^θ in this region (67.5°E)
306 and zonal mean when compared to the scenario with the idealized warm pool. The peak power
307 for the stochastic model simulations also occurs at slightly lower frequencies than the MJO-
308 mode dispersion curves, similar to *Thual et al.* [2014]. In addition, there are secondary peaks in
309 $\overline{H}a$ and u at double and triple the MJO-mode frequencies, both of which are likely attributed to
310 the nonlinear qa term in the skeleton model.
311 Figure 4 shows the leading two structures from a univariate EOF analysis of the
312 convective heating and zonal wind for Case-WP. While the variance in convective heating, $\overline{H}a$,
313 is centered over the longitudes with the maximum forcing for the idealized warm pool case
314 (Figure 1a), the EOF structures for the univariate analysis show significant noise due to the
315 inclusion of stochastic effects (Figures 4a and 4b), even after having already applied a 20-100

316 day filter. Furthermore, EOF1 and EOF2 only each explain 3.4% of the observed variance
317 despite using a sufficiently long record of approximately 340 years of simulation data. Although
318 the skeleton model is already computed on a relatively coarse grid (625 km or 5.625°) the
319 stochastic processes in the model occur at scales too small to identify recurring modes with the
320 simple global EOF analysis without additional smoothing first being applied to the model data.
321 The leading structures from the univariate zonal wind analysis for Case-WP show a highly
322 symmetric wavenumber-1 pattern centered about the maximum of the idealized warm pool with
323 31.3% of the variance explained by the leading two modes. The third and fourth EOF structures
324 for Case-WP identify a wavenumber-2 circulation anomaly centered about the warm pool
325 maximum that explain an additional 16.2% of the combined variance (not shown).
326 The first two modes from the multivariate EOF analysis for Case-WP are shown in
327 Figures 5a and 5b. The order of the leading EOFs has been switched to better facilitate
328 comparisons with the observed EOF patterns from *Wheeler and Hendon* [2004], which are
329 plotted for reference in Figures 5c and 5d. The EOF structures for the convective heating
330 anomalies improve significantly when constrained by the variations in zonal wind for the
331 combined analysis with a clear zonal wavenumber-1 pattern of enhanced heating and cooling (cf.
332 Figures 4a-4b and Figures 5a-5b). Albeit, the previous increase comes at the expense of a
333 reduction in the total explained variance, which is only 16.7% for the combined EOF analysis.
334 The heating EOFs have a maximum correlation coefficient of 0.70 and 0.68 with the observed
335 *Wheeler and Hendon* [2004] OLR EOFs (Figures 5c and 5d) when calculated at all longitudes in
336 order to account for any displacement in the maximum amplitude (Table 1). The zonal wind
337 structures in the multivariate analysis are nearly identical to the univariate patterns, suggesting
338 that the combined index is likely far more sensitive to the circulation component alone as is the

339 case in observations [e.g., *Straub*, 2013]. The multivariate circulation modes generally mimic the
340 structures in the observed *Wheeler and Hendon* [2004] EOFs with a maximum correlation of
341 0.83 and 0.72 (Table 1), though the observed EOF patterns contain more asymmetry and explain
342 a higher percent of the total variance (25.0%) than Case-WP from the skeleton model.
343 Regardless, it is impressive the skeleton model is able to reproduce the salient features of the
344 observed RMM index considering the many simplifications in the model and the use of an
345 idealized warm pool in lieu of observed SSTs.

346 The equivalent multivariate EOF modes for the skeleton model realization using the
347 truncated, observed SSTs (Case-SST8N) are shown in Figures 6a and 6b. As compared to Case-
348 WP, the addition of the observed s^q and s^θ increases the asymmetry in the convective heating and
349 zonal wind structures and better matches the observed *Wheeler and Hendon* [2004] EOFs
350 (Figures 6c and 6d). As such, the maximum correlation coefficient between the model and
351 observed EOFs increases from 0.70 and 0.68 (Case-WP) to 0.89 and 0.80 (Case-SST8N) for the
352 convective heating variable (Table 1). Likewise, the correlation for the circulation anomalies
353 increases from 0.83 and 0.72 to an incredible 0.98 and 0.94 for Case-WP and Case-SST8N,
354 respectively (Table 1) As in Case-WP, the model EOF structures are in quadrature with the
355 maximum cross-correlation (i.e., between the corresponding principal components) for Case-
356 SST8N at 9 days (Figure 7), consistent with observations and suggesting an overall MJO
357 oscillation frequency of ~40 days.

358 The peak positive values in zonal wind for the Case-SST8N multivariate EOFs are
359 located about 30-40° east of where the maxima occur in observations. The combined EOFs also
360 explain 15.7% of the total variance, which is slightly lower than for Case-WP. Nevertheless, the
361 multivariate EOFs bear a striking resemblance to the observed EOF patterns from the RMM

362 index, with maximum correlations of 0.98 and 0.94 for the circulation component and 0.89 and
363 0.80 for the convection anomalies (Table 1). As such, we therefore choose to routinely project
364 the model data directly onto the *Wheeler and Hendon* [2004] EOFs when calculating the model
365 principal components (i.e., hybrid SMM1 and SMM2 values that depend on both the model and
366 observations) in order to directly evaluate how well the skeleton model is able to reproduce
367 observed MJO event statistics using the RMM framework. The use of a reference set of EOFs for
368 calculating the model principal components also provides a valuable standard and better
369 facilitates comparison of MJO climatology statistics among different model solutions using
370 varying parameters or forcing data.
371
372 *3.2. Identifying MJO Events in the Skeleton Model*
373 Having already developed an RMM-like index that is similar to observations, we now
374 turn our attention to applications of the SMM index, including the identification of MJO events
375 in the skeleton model. Similarly, we also document the sensitivities of using a univariate, model-
376 derived multivariate, and the *Wheeler and Hendon* [2004] observed multivariate EOFs for the
377 resulting MJO event climatology.
378 This study uses the common practice of one standard deviation (i.e., a combined SMM
379 amplitude greater than or equal to unity) as a lower threshold for defining the presence of a
380 strong MJO. In addition, we employ the technique used in *Stachnik et al.* [2015], where the daily
381 values of SMM1 and SMM2 must contain nearly continual counter-clockwise rotation (i.e.,
382 eastward propagation) in the 2-dimensional phase space of *Wheeler and Hendon* [2004] and
383 require that an MJO "event" pass through at least four phases of the SMM index.

Two examples of MJO events waves are shown in Figure 8 for Case-WP. For each event, the SMM index was calculated by projecting the skeleton model data onto the multivariate, observed *Wheeler and Hendon* [2004] EOFs. Using the above definition, an MJO event initiates on day 30564 and day 32665 for the periods in Figures 8a and 8b and are noted with a gray circle for the first days when the combined SMM amplitude grows above 1.0 along the far eastern edge of the RMM phase 8 domain and western region of RMM phase 6, respectively. The MJO event in Figure 8a begins to propagate eastward through two phases (RMM phase 8 and phase 1) before being officially identified as a continuing or pre-existing MJO event provided it continue to propagate through four additional phases and is highlighted in blue. These conditions are met again as the MJO moves into the RMM phase 3 and phase 4 domains, each counting as a separate continuing MJO event (in contrast to primary events that develop from inactive conditions) with the subsequent paths colored in light and dark green, respectively. For simplicity, only the first day of the continuing events are shown in Figure 8b, with a special circumnavigating event or wave train MJO denoted in gold for RMM phase 6 when the MJO has successfully propagated around all longitudes. As such, the initiation of each primary MJO may contain multiple continuing events, especially for very long-lasting MJOs.

Termination events occur when the SMM amplitude decays below unity for an extended period of time or demonstrates significant westward propagation. Examples of MJO termination events are shown in RMM phase 7 and phase 1 for Figures 8a and 8b, respectively. Overall, the event histories are much smoother than in observations [e.g., Figure 1 in *Stachnik et al.*, 2015], implying that the day-to-day noise and high frequency variability that may be caused by the presence of other convectively coupled equatorial waves is likely dampened in the SMM index due to the additional step of including a high-pass filter that is not done for the RMM index [e.g.,

407 *Roundy et al.*, 2009]. Additional details and sensitivities of the search algorithm are described in
408 *Stachnik et al.* [2015].

409 Table 2 lists the number of MJO events from 34 years of observations (1979-2012) using
410 the historical RMM index and the mean and 95% confidence intervals for an equivalent 34 year
411 period derived from 680 years of skeleton model data for the simulation using an idealized warm
412 pool (Case-WP). Overall, the number of model MJO events is in fairly good agreement with
413 observations when one considers the highly idealized form of the model and the lack of model
414 tuning relative to this metric. In detail, for all methods of calculating the SMM index (i.e.,
415 univariate, multivariate model EOFs, and multivariate observed EOFs) the number of primary
416 MJOs is less than observations with a range 89.3-97.7 events for the skeleton model compared to
417 154 events in observations. The uncertainty estimates for primary MJO events are fairly small,
418 with a limited range of 3.6-4.8% relative to the mean number of events. With the exception of
419 the univariate zonal wind EOF analysis, the mean number of continuing events exceeds
420 observations, though the observed number falls within the 95% confidence intervals in each case.
421 Similarly, all of the Case-WP scenarios contain approximately 40-60% more circumnavigating
422 events than actually occur. Finally, the number of terminating events is identical to the primary
423 MJOs, as all events that initiate must eventually come to an end in the skeleton model.

424 The decrease in the number of separate MJO events in the skeleton model while
425 maintaining a nearly equal or slightly greater number of continuing and circumnavigating events
426 implies that the average MJO event length (measured as the number of days between event
427 initiation and termination) should be higher in the model than observations. This presumption is
428 correct, with a mean model event length of about 40 days for all realizations from Case-WP in
429 contrast to an approximate 35 day event length in observations (Table 2). Also, it is interesting to

note that there is little overall sensitivity to method of selecting EOFs when creating the model event climatology. Nevertheless, using the observed *Wheeler and Hendon* [2004] EOFs resulted in the most favorable comparison for primary MJOs with those seen in nature.

Similar results for the number of MJO events and average MJO event length are provided in Table 3 for the case using the truncated, observed SSTs (Case-SST8N). Once again, the number of primary MJOs is less than in observations, with only about 64% the number of observed MJOs regardless of the choice in EOFs. Here, the percent increase in the number of continuing and circumnavigating events is higher than for Case-WP, with 443.5-477.9 continuing events and 33.4-36.6 circumnavigating MJOs in the skeleton model compared to 330 and 15 MJO events in observations, respectively. As a result, the average MJO event length for Case-SST8N is higher than the idealized warm pool simulation, with an average length of approximately 44 days.

The increase in the average MJO event length for the skeleton model simulations is somewhat deceptive, however, as further investigation revealed that the mean event length is primarily skewed by a smaller number of simulated MJO events that have very long length. Figure 9 shows the cumulative probability distribution function of the observed and modeled MJO event lengths for a representative 34 year period of the simulation using the truncated, observed SSTs. In actuality, the shortest 40-50% of simulated MJO events in the stochastic model match observations (Figure 9).

Moreover, the introduction of stochasticity in the model is critical for generating a more realistic MJO event climatology. Additional simulations using the deterministic version of the model with the idealized warm pool or observed SSTs (Case-WPdet and Case-SST8Ndet, respectively) showed about a 10% reduction in the number of primary MJOs compared to their

453 stochastic simulations with an approximate 130% and 175% increase in the number of
454 continuing events for the deterministic solutions in Case-WPdet and Case-SST8Ndet,
455 respectively (Table 4). The resulting average MJO event lengths for the deterministic solutions
456 far exceeds observations, with Figure 9 indicating a significant positive bias for all MJO event
457 lengths for a representative 34 year period of Case-SST8Ndet. In fact, nearly 10% of simulated
458 MJOs last more than 150 days in this case.
459
460 *3.3. Geographic Distribution of MJO Events in the Skeleton Model*
461 Thus far, the use of real data SSTs in the skeleton model has been shown to produce more
462 realistic multivariate EOF structures with higher correlation values that better match the
463 observed *Wheeler and Hendon* [2004] RMM EOFs. Furthermore, those model simulations using
464 the annual average SSTs (Figure 2) or observed forcing [*Ogrosky and Stechmann*, 2015] produce
465 a more realistic geographic distribution of convective heating with an increase in $\overline{Ha}$ variance
466 over the locations where it is actually observed. Therefore, it becomes reasonable to wonder how
467 zonal variations in the external forcing terms might alter the geographic distribution of MJO
468 initiation and termination events in the skeleton model. Prior to applying this test for natural
469 climate variability states such as the modulations in the forcing distribution due to ENSO or
470 Indian Ocean Dipole (IOD) SSTs, it is first necessary to determine whether or not the skeleton
471 model can reproduce the observed geographic variability of MJO initiation and termination
472 events using annual average SSTs.
473 Figure 10 shows the relative frequency of occurrence for primary, continuing, and
474 terminating MJO events subset by RMM phase for 34 years of observations and similar periods
475 of skeleton model data for Case-WP, Case-SST8N, and Case-SST8Ndet. While the figures are

476 similar to the 2-dimensional phase space diagrams from *Wheeler and Hendon* [2004], the plots
477 indicate the percent likelihood of each MJO event type visualized in a radial-frequency domain.
478 On average, MJO events are most likely to initiate over the Indian Ocean (RMM phase 2 and
479 phase 3) and terminate over the Western Pacific or western hemisphere (RMM phase 6 and
480 phase 8), as evidenced for observations in Figure 10a. Figure 10b shows an analogous
481 distribution for a single 34 year period for Case-WP using the observed *Wheeler and Hendon*
482 [2004] EOFs when calculating the corresponding event climatology. There is some suggestion
483 that the simulated MJOs prefer to initiate in the RMM phase 1 and phase 2 domains, with local
484 termination maxima in RMM phase 8 and phase 5 (i.e., western hemisphere and exiting the
485 Maritime Continent, respectively). Comparisons for Case-SST8N (Figure 10c) are in less
486 agreement, however, with a large termination peak located within the RMM phase 3 domain that
487 does not match observations. The deterministic model simulation for this case (Case-SST8Ndet)
488 is also different from observations with the simulated MJOs becoming too regular and
489 preferentially beginning and terminating in RMM phase 3 and phase 2, respectively (Figure
490 10d).

491 To better determine whether or not the skeleton model is capable of reproducing the
492 observed MJO event climatology as a function of the large-scale forcing, we extend the previous
493 analysis to 680 years of model data, i.e., 20 independent samples of 34 year periods similar in
494 length to the observations. Figure 11 displays the mean event frequencies and 95% confidence
495 intervals as a function of RMM phase for the observations and a number of different model
496 simulations. In all panels, the uncertainty is calculated using a binomial proportion confidence
497 interval that is dependent on the pass and fail rates of the N events being assigned to a particular
498 RMM phase throughout the entire record. As such, the results are only statistically significant if

499 the confidence intervals and error bars do not overlap the reference line of 12.5%, i.e., the equal
500 likelihood that an MJO event will occur within any of the eight RMM phases.

501 Unfortunately, most of the observations in Figure 11a cannot be treated as statistically
502 significant or different from an equal chance due to the relatively large confidence intervals and
503 shorter historical record of observed MJOs. The skeleton model, however, is not constrained by
504 the lack of samples and can be run for extended periods. As a check, we perform the same
505 analysis on a special long-term stochastic simulation using a homogenous background (Case-
506 HG) where the principal components are calculated using the model's own EOFs. This situation
507 should be most likely to produce equal chance results for all RMM phases, which is successfully
508 recovered in Figure 10d. Only a few of the mean frequencies for Case-WP or Case-SST8N
509 (Figures 10b and 10c) demonstrate any statistical significance from an equal probability and the
510 bumps in the MJO event distributions do not necessarily match observations. It remains possible,
511 however, that the stochastic effects in the model act to dilute the geographic signal and impacts
512 of applying zonally varying forcing. The long-term climatology for Case-WPdet does show some
513 features in common with the locations of MJO event initiation and are statistically significant yet
514 demonstrate little skill for the corresponding climatology of termination events (Figure 11e). The
515 frequency distribution for Case-SST8Ndet produces the largest differences from an equal chance,
516 though those phases with distinguishable frequencies do not match observations (Figure 11f). As
517 such, more work is needed to help separate the effects of nonlinearity, stochasticity, and zonally-
518 varying forcing upon where MJO events begin and decay in the skeleton model. Similarly, the
519 model may need to account for other factors such as interactions with the extratropical
520 circulation before making any firm conclusions regarding its potential future use in studying
521 natural climate variability and change.

522

523 *3.4. Composites and Precursors for MJO Initiation and Termination*

524 Figure 12 shows the composite RMM1-RMM2 indices associated with primary MJO
525 event initiation for all phases in observations and the corresponding SMM1-SMM2 histories
526 from a single 34 year period of skeleton model data for Case-WP, Case-SST8N, and Case-
527 SST8Ndet. The observed *Wheeler and Hendon* [2004] EOFs were used to calculate the principal
528 components in each model case and the day 0 (i.e., first day with combined amplitude greater
529 than 1.0) is noted with a circumscribed X in all panels.

530 In the observations and stochastic simulations, MJO initiation occurs rather quickly, with
531 a rapid increase in the combined RMM and SMM amplitudes for the three days prior to the
532 eventual initiation. The observational composite shows continued growth for an additional 2-3
533 days with most phases achieving a near constant value with only weak growth of the combined
534 amplitude through the following 12 days (Figure 12a). Meanwhile, the stochastic simulations
535 share the same initial growth (i.e., rapid intensification for 3 days prior to initiation) though
536 continue to intensify beyond the observed values of RMM amplitude and reach a maximum
537 SMM amplitude 5-6 days after the initiation of an event (Figures 12b and 12c). Overall, the
538 average root-mean-square error (RMSE) for all eight phases is 0.27 and 0.23 amplitude units for
539 Case-WP and Case-SST8N, respectively. The initiation composite for the deterministic model
540 simulation follows the same trend as the observations and stochastic runs although the SMM
541 amplitude growth rates are much slower before and after the MJO initiation (Figure 12d).
542 Consequently, the smaller changes in SMM amplitude for Case-SST8Ndet result in the largest
543 values of RMSE (0.29 amplitude units) and do not match the observations as well at the
544 stochastic simulations.

545 Analogous RMM and SMM composites are shown before and after the start of an MJO
546 termination event in Figure 13. Again, 2-3 days seems to be the relevant time scales for the
547 decay of an observed MJO event as the combined RMM amplitudes maintain near constant
548 values in the composite until approximately 3 days prior to the termination markers that indicate
549 the last day where the combined amplitude remains above unity (Figure 13a). Only RMM phase
550 2 termination events seem to experience gradual decay, with the RMM amplitude weakening for
551 about 7 days prior to termination [*Stachnik et al.*, 2015]. The composites for the stochastic model
552 simulations attain stronger values of SMM amplitude 5-6 days prior to the eventual termination
553 event than seen in observations (Figures 13b and 13c). The average RMSE values are 0.27 and
554 0.26 for Case-WP and Case-SST8N, respectively. As with initiation, the changes in SMM
555 amplitude for Case-SST8Ndet occur more slowly are much smaller than actually observed
556 (Figure 13d). However, the RMSE for the deterministic run is slightly smaller (0.24 amplitude
557 units) given the pronounced pulsing in SMM amplitude prior to termination for the stochastic
558 simulations during this period.
559 Figure 14 attempts to identify possible mechanisms for MJO termination and shows the
560 lag-longitude composites of the anomalous convective heating, moisture, and zonal wind at the
561 equator from Case-SST8N using the observed *Wheeler and Hendon* [2004] EOFs for
562 approximately 340 years of MJO events that either continue or terminate in the RMM phase 6
563 region. All of the model variables have been time filtered to isolate the 20-100 day intraseasonal
564 variability. Differences between the continuing and terminating events are shown for each
565 variable in the bottom panel of each column along with stippling indicating the presence of a
566 statistically significant different mean associated with continuing and terminating MJOs.

567 To begin, the differences in the large-scale environmental conditions at positive lags (i.e.,
568 after the termination of an MJO event) are not nearly as pronounced as they are in observations
569 [cf. Figure 4 in *Stachnik et al.*, 2015]. For example, the zonal wind maintains a wavenumber-1
570 type circulation anomaly after day 0 for the terminating cases in the skeleton model (Figure 14h)
571 with the main difference being a weaker amplitude than identified during positive lags for the
572 continuing events (Figure 14g). Conversely, the wavenumber-1 circulation anomaly decays
573 rapidly when compositing low-level zonal winds from reanalysis data for terminating MJO
574 events [Figure 4 in *Stachnik et al.*, 2015]. In addition, there is no single variable that seems to
575 best predict whether an MJO event will continue or terminate once entering the RMM phase 6
576 domain. Unlike in observations, significant differences between continuing and terminating
577 events occur in both the active and inactive phases of the MJO for the $\overline{Ha}$, q, and u anomalies.
578 These difference appear to manifest within MJO wave trains and are identifiable more than 30
579 days prior to the eventual continuing or terminating event. The above result is intriguing,
580 considering that the composite SMM indices in Figure 13 only suggest a weakening of the
581 SMM1-SMM2 amplitudes in the 5-6 days immediately prior to event termination. As such, it is
582 not immediately clear what sort of physical precursor conditions may be affecting MJO
583 termination in the skeleton model.
584 Figure 15 expands the above analysis to include composites and differences in
585 convergence and potential temperature for the 340 year period of continuing and terminating
586 MJOs with the rightmost column showing potential temperature composites for a shorter, single
587 34 year period of skeleton model data. Once more, the differences in convergence and potential
588 temperature at positive lags for terminal events is more closely related to amplitude differences
589 rather than a complete shutdown of the large-scale pattern. However, it is interesting to note that

590 there are a number of slow moving (~1 m s^{-1}), eastward propagating waves embedded within the
591 composite difference panels for the convergence and potential temperature in Figures 15c and
592 15f. These anomalies occur at relatively high wavenumber ($k \approx$ 12-13) are even more
593 pronounced in the termination composites for the shorter 34 year period (cf. Figures 15g and
594 15h). *Majda and Stechmann* [2011] noted the potential interaction of dry Kelvin and Rossby
595 modes during MJO termination for the skeleton model, though the waves in our analysis travel
596 much more slowly than these theoretical modes. The previous suggests that continuing MJO
597 events may suppress the development of eastward propagating waves, or alternatively, the
598 emergence of dry Kelvin or other higher wavenumber modes embedded within the large-scale
599 flow may interfere with MJO dynamics and help lead to its future demise.
600 Finally, Figure 16 shows the distribution of zonal wind and moisture anomalies for
601 individual RMM phase 6 MJOs averaged over the local domain (120-160°E) at 10 days prior to
602 the continuing or terminating event for Case-SST8N. As is the case with observations in
603 *Stachnik et al.* [2015], there is appreciable overlap in the anomaly distributions for individual
604 continuing and terminating events despite containing a statistically significant different mean for
605 the time and longitudes displayed (e.g., Figure 14i). For example, individual continuing MJO
606 events may contain cooling and drying whereas terminating events may experience moistening
607 and warming (Figure 16b). Subsequently, there appears to be no one recurring or unique set-up
608 for MJO termination even in the relatively simple and low-order stochastic skeleton model.
609
610 **4. Summary and Discussion**
611 This study developed an RMM-like index for the deterministic and stochastic version of
612 the MJO skeleton model [*Majda and* Stechmann, 2009; 2011] using the basic approach outlined

613 in *Wheeler and Hendon* [2004]. Univariate and multivariate EOF analyses were performed using
614 convective heating and zonal wind data taken from the skeleton model simulations forced with
615 an idealized warm pool and observed SSTs. The simulations with the observed SSTs (Case-
616 SST8N) demonstrated a number of small improvements over the idealized warm pool (Case-
617 WP), including greater variance of the convective heating over the locations where it is actually
618 observed and was consistent with the observationally-motivated skeleton model simulations
619 performed by *Ogrosky and Stechmann* [2015]. Moreover, the leading modes of the multivariate
620 EOF analysis from Case-SST8N had greater correlations than the corresponding modes from
621 Case-WP and contained zonal asymmetries that closely resembled the observed *Wheeler and*
622 *Hendon* [2004] RMM EOFs. Overall, the leading EOFs for the multivariate analysis of Case-
623 SST8N showed a wavenumber-1 convectively-coupled circulation anomaly that explained 15.7%
624 of the total variance. The skeleton multivariate MJO (SMM) index also appeared to rely more
625 heavily on the circulation component, as is the case in observations [e.g., *Straub*, 2013], given
626 the lack of a well-defined univariate EOF mode for convective heating in the model data.
627 A climatology of MJO events was performed using the SMM index similar to that for
628 observations in *Stachnik et al.* [2015]. It was shown that the stochastic skeleton model produces
629 a number of MJO events that, for such a simple model, compares reasonably well with the
630 observed number of MJO events. As such, the average MJO event length in the model was
631 approximately 40 days and 44 days for Case-WP and Case-SST8N, respectively, which is only
632 slightly higher than in observations (~35 days). Distributions of the average event length
633 revealed that the skeleton model does a good job of simulating the shortest 40-50% of MJO
634 events but the average length is skewed by the occasional presence of very long MJOs not seen
635 in nature, suggesting that the stochastic parameters used in the model are well-tuned. The

existence of additional circumnavigating and long-lasting MJOs in the model is reasonable, however, given the lack of damping on the planetary scale and the omission of other factors such as enhanced friction over land surfaces that may help terminate observed events. The total number of MJOs and corresponding event lengths were relatively insensitive to the choice of EOFs (e.g., model univariate, multivariate, or the observed RMM patterns) used to calculate the SMM index.

An initial attempt was made to quantity the geographic distributions of MJO event initiation and termination based on the large-scale forcing. Whereas most of the model quantities were relatively stable for shorter periods that mimicked the length of observations (34 years), the frequencies of MJO initiation in a given RMM phase varied strongly over shorter time periods and required a much longer record (680 years) for analysis. While the simulated climatology for shorter periods may occasionally resemble observations, the long-term record for the stochastic model simulations showed nearly equal chance for an MJO event to initiate or terminate in any RMM phase despite the existence of zonal variations in the external radiative cooling and moistening terms used to force the model. The deterministic solutions did show statistically significant preferred regions of MJO initiation and termination for the long-term analysis, though these features did not always match observations.

The previous finding presents a bit of conundrum, considering that using observed SSTs to force the model results in a more realistic representation of the mean convective heating and variance that is in agreement with *Ogrosky and Stechmann* [2015] while also producing multivariate EOF structures that more closely resemble the observed RMM patterns taken from *Wheeler and Hendon* [2004]. Despite this fact, the stochastic simulation using the observed SSTs provided no improvement over the idealized warm pool case for accurately simulating the

observed geographic variability of MJO events. The effect of stochasticity here appears to distribute MJO events more equally throughout the domain. Regardless, MJOs initiate and terminate in all RMM phases in the deterministic model simulations, albeit some phases were preferred that did not necessarily match observations.

While the basic model assumptions and observed, annual average SSTs may be sufficient to generate reasonable looking MJO dynamics, structures, and number of events, additional factors beyond internal tropical variability and the climatological forcing may be required to produce realistic distributions of MJO initiation and decay. For example, MJOs may initiate from any number of mechanisms including influences from higher latitudes such as cold air outbreaks and Rossby wave trains [e.g., *Hsu et al.*, 1990; *Matthews and Kiladis*, 1999; *Ray and Zhang*, 2010; *Wang et al.*, 2012] or topographic effects [e.g., *Hsu and Lee*, 2005], all of which have geographic variability that are not accounted for in the skeleton model. Future work will continue to evaluate long-term records of simulated MJO behavior from the skeleton model as a function of the shape and strength of the tropical warm pool in order to determine if the model is capable of identifying shifts in the location or lifetimes of MJO events as a function of ENSO [e.g., *Pohl and Matthews*, 2007] or Indian Ocean dipole SSTs.

The effects of stochasticity were also necessary for the model to produce more realistic estimates for the time scales of MJO event initiation and termination. The introduction of the stochastic parameterization is to better account for the random component of the growth and decay of unresolved synoptic and mesoscale convective processes that occur within the MJO envelop. These processes are needed here, and in nature, to accelerate the time scales of initiation and decay that are otherwise too slow through the neutrally stable wave interactions and large-scale moisture depletion that occurs in the deterministic version of the skeleton model. In fact,

682 almost every one of the stochastic model simulations produced a more realistic looking MJO
683 initiation and termination composite with smaller RMSE values regardless of the choice of EOFs
684 when calculating the principal components or background forcing when compared to a
685 corresponding deterministic solution (not shown).

686 Finally, we examined the large-scale conditions associated with the termination of MJO
687 events in the skeleton model over the RMM phase 6 domain. As previously reported through a
688 visual analysis of MJO time series in *Majda and Stechmann* [2009, 2011] and *Thual at al.*
689 [2014], the skeleton model produced MJO events that either stall or experience decay
690 immediately upstream or directly over the warm pool maximum as observed in nature. However,
691 it is important to note that these successes may not be for the correct physical reasons, as the
692 observed MJO encounters a number of additional factors that may weaken it over this domain
693 that are not accounted for in the skeleton model such as stronger diurnal cycles, topographic
694 effects, and enhanced boundary layer friction over land. Moreover, our analysis of the precursor
695 conditions associated with MJO decay in the skeleton model indicated that higher wavenumber
696 ($k \approx$ 12-13) oscillations embedded within the large-scale flow may affect MJO termination.
697 Whether the development of these waves are either suppressed by continuing MJO events, or
698 alternatively, the emergence of the dry Kelvin and higher-frequency waves contribute towards
699 MJO event termination remains unknown. Our future work plans to examine the wave power
700 spectra associated with MJO termination events in observations and the skeleton model to better
701 elucidate what mechanisms may be responsible for MJO initiation and decay.

Acknowledgments

The RMM index was obtained from the Australian Bureau of Meteorology website. The NOAA OI SST v2 data were provided by the NOAA/Office of Oceanic and Atmospheric Research (OAR)/Earth System Research Laboratory (ESRL) Physical Sciences Division (PSD) in Boulder, CO, USA, and obtained from their website at http://www.esrl.noaa.gov/psd/. Part of this research was carried out at the Jet Propulsion Laboratory, California Institute of Technology, under a contract with the National Aeronautics and Space Administration. This study was funded by the Office of Naval Research (ONR) award number N00014-12-1-0912.

711 **References**

712 Ajayamohan, R. S., B. Khouider, and A. J. Majda (2013), Realistic initiation and dynamics of the
713 Madden-Julian oscillation in a course resolution aquaplanet GCM, *Geophys. Res. Lett.*,
714 *40*, 1-6, doi:10.1002/2013GL058187.

715 Bechtold, P., M. Köhler, T. Jung, F. Doblas-Reyes, M. Leutbecher, M. J. Rodwell, F. Vitart, and
716 G. Balsamo (2008), Advances in simulating atmospheric variability with the ECMWF
717 model: From synoptic to decadal time-scales, *Q. J. Roy. Meteor. Soc.*. *134,* 1337–1351,
718 doi: 10.1002/qj.289.

719 Benedict, J. J., E. D. Maloney, A. H. Sobel, D. M. Frierson, and L. J. Donner (2013), Tropical
720 intraseasonal variability in version 3 of the GFDL atmosphere model, *J. Climate*, *26*,
721 426–449.

722 Benedict, J. J., and D. A. Randall (2009), Structure of the Madden–Julian oscillation in the
723 superparameterized CAM, *J. Atmos. Sci.*, *66*, 3277-3296.

724 Bond, N. A., and G. A. Vecchi (2003), The influence of the Madden–Julian oscillation on
725 precipitation in Oregon and Washington, *Wea. Forecasting*, *18*, 600-613.

726 Chen, Y.-H., and A. D. Del Genio (2009), Evaluation of tropical cloud regimes in observations
727 and a general circulation model, *Climate. Dyn.*, *32*, 355-369.

728 Deng, Q., B. Khouider, and A. J. Majda (2015), The MJO in a coarse-resolution GCM with a
729 stochastic multicloud parameterization, *J. Atmos. Sci.*, *72*, 55–74.

730 Goswami, B. N., and R. S. Ajaya Mohan (2001), Intraseasonal oscillations and interannual
731 variability of the Indian summer monsoon, *J. Climate*, *14*, 1180-1198.

732 Grabowski, W. W. (2003), MJO-like coherent structures: Sensitivity simulations using the cloud-
733 resolving convection parameterization (CRCP), *J. Atmos. Sci.*, *60*, 847-864.

734 Guan, B., D. E. Waliser, N. P. Molotch, E. J. Fetzer, and P. J. Neiman (2012), Does the Madden–
735 Julian oscillation influence wintertime atmospheric rivers and snowpack in the Sierra
736 Nevada?, *Mon. Wea. Rev.*, *140*, 325–342.
737 Hannah, W. M., and E. D. Maloney (2011), The role of moisture–convection feedbacks in
738 simulating the Madden–Julian oscillation, *J. Climate*, *24*, 2754–2770.
739 Hendon, H., H., and M. L. Salby (1994), The life cycle of the Madden–Julian oscillation, *J.*
740 *Atmos. Sci.*, *51*, 2225-2237.
741 Higgins, R. W., J.-K. E. Schemm, W. Shi, and A. Leetmaa (2000), Extreme precipitation events
742 in the western United States related to tropical forcing, *J. Climate*, *13*, 793-820.
743 Hsu, H.-H., B. J. Hoskins, and F.-F. Jin (1990) The 1985/86 intraseasonal oscillation and the role
744 of the extratropics, *J. Atmos. Sci.*, *47*, 823-839.
745 Hsu, H.-H., and M.-Y. Lee (2005): Topographic effects on the eastward propagation and
746 initiation of the Madden–Julian oscillation, *J. Climate*, *18*, 795–809.
747 Hung, M.-P., J.-L. Lin, W. Wang, D. Kim, T. Shinoda, and S. J. Weaver (2013), MJO and
748 convectively coupled equatorial waves simulated by CMIP5 climate models, *J. Climate*,
749 *26*, 6185-6214.
750 Huffman, G. J., R. F. Adler, D. T. Bolvin, and G. Gu (2009), Improving the global precipitation
751 record: GPCP version 2.1. *Geophys. Res. Lett.*, *36*, L17808, doi:10.1029/2009GL040000.
752 Jiang, X., et al. (2015), Vertical structure and physical processes of the Madden-Julian
753 oscillation: Exploring key model physics in climate simulations, *J. Geophys. Res. Atmos.*,
754 in press.

755 Jiang, X., M. Zhao, and D. E. Waliser (2012), Modulation of tropical cyclone activity by the
756 tropical intraseasonal oscillation over the Eastern Pacific in a high resolution GCM, *J.*
757 *Climate*, *25*, 6524-6538.
758 Kiladis, G. N., J. Dias, K. H. Straub, M. C. Wheeler, S. N. Tulich, K. Kikuchi, K.M.
759 Weickmann, and M. J. Ventrice (2014), A comparison of OLR and circulation based
760 indices for tracking the MJO, *Mon. Wea. Rev.*, *142*, 1697-1715.
761 Khouider, B., and A. J. Majda (2006), A simple multicloud parameterization for convectively
762 coupled tropical waves. Part I: Linear analysis, *J. Atmos. Sci.*, *63*, 1308-1323.
763 Khouider, B., and A. J. Majda (2007), A simple multicloud parameterization for convectively
764 coupled tropical waves. Part II: Nonlinear simulations, *J. Atmos. Sci.*, *64*, 381-400.
765 Khouider, B., A. St-Cyr, A. J. Majda, and J. Tribbia (2011), The MJO and convectively coupled
766 waves in a course-resolution GCM with a simple multicloud parameterization, *J. Atmos.*
767 *Sci.*, *68*, 240-264.
768 Klingaman, N. P., and S. J. Woolnough (2014a), The role of air–sea coupling in the simulation
769 of the Madden–Julian oscillation in the Hadley Centre model, *Q. J. Roy. Meteor. Soc.*.
770 *140*, 2272–2286, doi:10.1002/qj.2295.
771 Klingaman, N. P., and S. J. Woolnough (2014b), Using a case-study approach to improve the
772 Madden–Julian oscillation in the Hadley Centre model, *Q. J. Roy. Meteor. Soc.*, *140*,
773 2491–2505, doi:10.1002/qj.2314.
774 Lau, K.-M., and P. H. Chan (1986), Aspects of the 40–50 day oscillation during the northern
775 summer as inferred from outgoing longwave radiation, *Mon. Wea. Rev.*, *114*, 1354-1367.
776 Lau, W. K. M., and D. E. Waliser (2005), Intraseasonal Variability in the Atmosphere-Ocean
777 Climate System, Springer, Heidelberg, Germany.

778 Madden, R. A., and P. R. Julian (1971), Detection of a 40-50 day oscillation in the zonal wind in
779 the tropical Pacific, *J. Atmos. Sci.*, *28*, 702-708.
780 Madden, R. A., and P. R. Julian (1972), Description of global-scale circulation cells in the
781 tropics with a 40–50 day period, *J. Atmos. Sci.*, *29*, 1109-1123.
782 Madden, R. A., and P. R. Julian (1994), Observations of the 40-50-day tropical oscillation – A
783 review, *Mon. Wea. Rev.*, *122*, 814-837.
784 Majda, A. J., and R. Klein (2003), Systematic multiscale models for the tropics, *J. Atmos. Sci.*,
785 *60*, 393-408.
786 Majda, A. J., and S. N. Stechmann (2009), The skeleton of tropical intraseasonal oscillations,
787 *Proc. Natl. Acad. Sci. USA, 106*, 8417-8422.
788 Majda, A. J., and S. N. Stechmann (2011), Nonlinear dynamics and regional variations in the
789 MJO skeleton, *J. Atmos. Sci.*, *68*, 3053-3071.
790 Maloney, E. D., and D. L. Hartmann (1998), Frictional moisture convergence in a composite life
791 cycle of the Madden–Julian oscillation, *J. Climate*, *11*, 2387–2403.
792 Maloney, E. D., and D. L. Hartmann (2000), Modulation of eastern north Pacific hurricanes by
793 the Madden–Julian oscillation, *J. Climate*, *13*, 1451-1460.
794 Matthews, A. J. (2000), Propagation mechanisms for the Madden-Julian oscillation, *Quart. J.*
795 *Roy. Meteor. Soc.*, *126*, 2637-2651.
796 Matthews, A. J. (2004), Intraseasonal variability over tropical Africa during northern summer, *J.*
797 *Climate*, *17*, 2427-2440.
798 Matthews, A. J. (2008) Primary and successive events in the Madden-Julian oscillation, *Quart. J.*
799 *Roy. Meteor. Soc.*, *134*, 439-453.

800 Matthews, A. J. and G. N. Kiladis (1999), The tropical–extratropical interaction between high-
801 frequency transients and the Madden–Julian oscillation, *Mon. Wea. Rev.*, *127*, 661-677.
802 Myers, D. S., and D. E. Waliser (2003), Three-dimensional water vapor and cloud variations
803 associated with the Madden–Julian oscillation during northern hemisphere winter, *J.*
804 *Climate*, *16*, 929-950.
805 Ogrosky, H. R., and S. N. Stechmann (2015), The MJO skeleton model with observation-based
806 background state and forcing, *Quart. J. Roy. Meteor. Soc.*, in press.
807 Pohl, B., and A. J. Matthews (2007), Observed changes in the lifetime and amplitude of the
808 Madden–Julian oscillation associated with interannual ENSO sea surface temperature
809 anomalies, *J. Climate*, *20*, 2659-2674.
810 Pritchard, M. S., and C. S. Bretherton (2014), Causal evidence that rotational moisture advection
811 is critical to the superparameterized Madden–Julian oscillation, *J. Atmos. Sci.*, *71*, 800-
812 815.
813 Ray, P., and C. Zhang (2010), A case study of the mechanics of extratropical influence on the
814 initiation of the Madden–Julian oscillation, *J. Atmos. Sci.*, *67*, 515-528.
815 Reynolds, R.W., N. A. Rayner, T. M. Smith, D. C. Stokes, and W. Wang (2002), An improved in
816 situ and satellite SST analysis for climate, *J. Climate*, *15*, 1609-1625.
817 Roundy, P. E., C. J. Schreck III, and M. A. Janiga (2009), Contributions of convectively coupled
818 equatorial Rossby waves and Kelvin waves to the real-time multivariate MJO indices,
819 *Mon. Wea. Rev., 470*, 469-478.
820 Slingo, J. M., et al. (1996), Intraseasonal oscillations in 15 atmospheric general circulation
821 models: Results from an AMIP diagnostic subproject, *Climate Dynam*., *12*, 325-357.

822 Stachnik, J. P., D. E. Waliser, and A. J. Majda (2015), Precursor environmental conditions
823 associated with the termination of Madden-Julian oscillation events, *J. Atmos. Sci.*, *72*,
824 1908-1931.
825 Stechmann, S. N., and A. J. Majda (2015), Identifying the skeleton of the Madden-Julian
826 oscillation in observational data, *Mon. Wea. Rev.*, *143*, 395–416.
827 Stechmann, S. N., and H. R. Ogrosky (2014), The Walker circulation, diabatic heating, and
828 outgoing longwave radiation, *Geophys. Res. Lett.*, *41*, 9097-9105,
829 doi:10.1002/2014GL062257.
830 Straub, K. H. (2013), MJO initiation in the real-time multivariate MJO index, *J. Climate, 26*,
831 1130-1151.
832 Thual, S., and A. J. Majda (2015), A skeleton model for the MJO with refined vertical structure,
833 *Climate Dynam.*, submitted.
834 Thual, S., A. J. Majda, and S. N. Stechmann (2014), A stochastic skeleton model for the MJO, *J.*
835 *Atmos. Sci.*, *71*, 697-715.
836 Thual, S., A. J. Majda, and S. N. Stechmann (2015), Asymmetric intraseasonal events in the
837 stochastic skeleton MJO model with seasonal cycle, *Climate Dynam.*, in press.
838 Ventrice, M. J., M. C. Wheeler, H. H. Hendon, C. J. Schreck III, C. D. Thorncroft, and G. N.
839 Kiladis (2013), A modified multivariate Madden–Julian oscillation index using velocity
840 potential, *Mon. Wea. Rev.*, *141*, 4197–4210.
841 Waliser, D. E., C. Jones, J.-K. E. Schemm, and N. E. Graham (1999), A statistical extended-
842 range tropical forecast model based on the slow evolution of the Madden–Julian
843 oscillation, *J. Climate*, *12*, 1918-1939.
844 Waliser, D., et al. (2009), MJO simulation diagnostics, *J. Climate*, *22*, 3006–3030

845 Wang, L., K. Kodera, and W. Chen (2012), Observed triggering of tropical convection by a cold
846 surge: Implications for MJO initiation, *Q. J. Roy. Meteorol. Soc.*, *138*, 1740-1750.
847 Wheeler, M. C., and H. H. Hendon (2004), An all-season real-time multivariate MJO index:
848 Development of an index for monitoring and prediction, *Mon. Wea. Rev.*, *132*, 1917-
849 1932.
850 Wheeler, M. C., G. N. Kiladis, and P. J. Webster (2000), Large-scale dynamical fields associated
851 with convectively coupled equatorial waves, *J. Atmos. Sci.*, *57*, 613-640.
852 Yoneyama, K., C. Zhang, and C. N. Long (2013), Tracking pulses of the Madden–Julian
853 oscillation, *Bull. Amer. Meteor. Soc.*, *94*, 1871–-891.
854 Zhang, C. (2005), Madden-Julian oscillation, *Rev. Geophys.*, *43*, RG2003,
855 doi:10.1029/2004RG000158.
856 Zhang, C., M. Dong, S. Gualdi, H. H. Hendon, E. D. Maloney, A. Marshall, K. R. Sperber, and
857 W. Wang (2006), Simulations of the Madden-Julian oscillation in four pairs of coupled
858 and uncoupled models, *Climate Dynam.*, *27*, 573-592.

Figure Captions

Figure 1. The shape of (a) the idealized warm pool (i.e., Case-WP) and (b) annual average (1971-2000) NOAA OI SSTs v2 used to force the skeleton model. The observed SSTs have been meridionally averaged from 10°S-10°N with a Poisson relaxation and interpolated over missing data (i.e., land). The solid line in (b) indicates the average SSTs from all waves downscaled to the model resolution of 625 km. The dashed profile in (b) has been smoothed to only retain the first eight Fourier modes (Case-SST8N).

Figure 2. (a)-(c) Hovmöller diagrams of the anomalous 10-100 day filtered skeleton model variables for a 600 day period taken from the idealized warm pool simulation (Case-WP). All variables have daily resolution and are shown in dimensional units for the reconstructed (a) convective heating ($\overline{H}a$), (b) zonal wind (u), and (c) moisture (q) variables. (d)-(f) As in (a)-(c), but for the model simulation using the truncated, observed SSTs (Case-SST8N).

Figure 3. Zonal wavenumber-frequency power spectra of the (a) convective heating ($\overline{H}a$, K day^{-1}) and (b) zonal wind (u, m s^{-1}) for the idealized warm pool case (Case-WP) from the skeleton model. Shading indicates the base-10 logarithm for the reconstructed and dimensional variables taken at the equator for approximately 34 years of model data. The black circles mark the dispersion curves from a separate stability analysis of the linear waves in the skeleton model in the Indian Ocean (67.5°E). The dashed, black lines indicate periods of 30 and 90 days. (c)-(d) As in (a)-(b), but for the model simulation using the truncated, observed SSTs (Case-SST8N).

881 **Figure 4**. (a)-(b) The first two leading modes from a univariate EOF analysis of the 20-100 day
882 filtered convective heating ($\overline{H}a$) anomalies along the equator from approximately 340 years of
883 the idealized warm pool simulation (Case-WP). (c)-(d) As in (a)-(b), but for a univariate EOF
884 analysis of the zonal wind (u). The percent variance explained by each mode is shown in the
885 upper-right of each panel.
886
887 **Figure 5**. (a)-(b) The first two leading modes from a multivariate EOF analysis of the 20-100
888 day filtered convective heating ($-\overline{H}a$) and zonal wind (u) model anomalies along the equator
889 from approximately 340 years of the idealized warm pool simulation (Case-WP). The order of
890 EOF1 and EOF2 have been interchanged in addition to switching the sign of the convective
891 heating term to better match the *Wheeler and Hendon* [2004] EOFs. (c)-(d) The first leading two
892 modes from the observed multivariate analysis of *Wheeler and Hendon* [2004] showing the
893 15°S-15°N EOF structures of OLR and zonal wind at 850 hPa and 200 hPa (u850 and u200,
894 respectively). The percent variance explained by each mode is shown in the upper-right of each
895 panel.
896
897 **Figure 6**. (a)-(b) As in Figure 5, but for the model simulation using the truncated, observed SSTs
898 (Case-SST8N). Panels (c)-(d) are identical to Figure 5 to better facilitate comparison between the
899 modeled and observed EOFs.
900
901 **Figure 7**. Lag correlations between the corresponding PC1 and PC2 from the multivariate EOF
902 analysis of approximately 340 years of the model simulation using the truncated, observed SSTs
903 (Case-SST8N).

Figure 8. Examples of two MJO events using the skeleton multivariate MJO (SMM) index and the event criteria defined in *Stachnik et al.* [2015] for the model simulation using an idealized warm pool (Case-WP). The daily values of SMM1 and SMM2 (i.e., the principal components) are plotted as small dots for (a) day 30561-30619 and (b) day 32662-32734 in the 2-dimensional phase space obtained when projecting the model data onto the observed EOF patterns of *Wheeler and Hendon* [2004]. The initiation of a primary MJO event is shown in gray and indicated with a large, circumscribed X while the corresponding termination event is shown in red for each panel. Continuing MJO events are shown in blue and green in (a), with the subsequent history of the SMM index highlighted through the following four phases. The beginning of each continuing event are shown with a large, blue marker in (b) along with the start of a circumnavigating event and associated path highlighted in gold. Additional details and allowances provided by the identification algorithm are described in the text.

Figure 9. Cumulative probability distribution functions of the observed and modeled MJO event lengths from the stochastic model simulation using the truncated, observed SSTs (Case-SST8N), and a deterministic model simulation using the same SSTs (Case-SST8Ndet). The observed distribution is based on the historical *Wheeler and Hendon* [2004] RMM index from 1979-2012 and is represented by a thick, black line. The corresponding model event length distributions for similar 34 year periods are shown using thin, blue and red lines, respectively.

Figure 10. Radial-frequency diagrams showing the percent occurrence of MJO events as a function of RMM phase for (a) observations (1979-2012) and single 34 year periods from stochastic model simulations using (b) an idealized warm pool (Case-WP) and (c) the truncated,

observed SSTs (Case-SST8N). (d) As in (c), but for the deterministic model simulation using the truncated and observed SSTs (Case-SST8Ndet). The black dots plotted at the center angle of each phase indicate the frequency of occurrence and are connected only for the ease of viewing primary, continuing, and terminal MJO events (gray, blue, and red lines, respectively). Range rings represent the 1%, 5%, 10%, 15%, and 20% frequencies of occurrence from the center to edge of the diagram, respectively.

Figure 11. The mean frequency and uncertainty estimates of primary (gray), continuing (blue), and terminal (red) MJO events for each RMM phase in (a) observations and (b)-(f) approximately 680 years of model data. Simulations using an idealized warm pool and the truncated, observed SSTs (Case-WP and Case-SST8N, respectively) are shown in panels (b)-(c) with a special simulation using a homogeneous background state (Case-HG) in (d). Results from a deterministic version of the skeleton model using the idealized warm pool (Case-WPdet) and truncated, observed SSTs (Case-SST8Ndet) are shown in (e)-(f). The dashed line indicates the 12.5% frequency and represents the equal likelihood of an MJO event occurring in any phase. Error bars indicate the 95% uncertainty estimates and are calculated from a binomial proportion confidence interval (see text for details). The total number of primary/terminal and continuing events are indicated in the top right of each panel. All model simulations use the observed *Wheeler and Hendon* [2004] EOFs to calculate the principal components and corresponding MJO events with the exception of the homogeneous background case, which uses the multivariate EOFs obtained directly from the model data.

949 **Figure 12.** Initiation composites of the RMM1-RMM2 paths for (a) observations (1979-2012)
950 and SMM1-SMM2 for an equivalent 34 year period from the stochastic model simulations using
951 (b) an idealized warm pool (Case-WP) and (c) the truncated, observed SSTs (Case-SST8N). (d)
952 As in (c), but for the deterministic model simulation using the truncated and observed SSTs
953 (Case-SST8Ndet). The composite values for a primary event are marked with a circumscribed X
954 for each phase. The composite history before (3 days) and after (12 days) the initiation event
955 (i.e., first day after the combined amplitude grows above unity) are shown in different colors for
956 each phase. The composite daily RMM and SMM values are plotted using small dots, while
957 closed squares appear every three days for reference.
958
959 **Figure 13.** As in Figure 12, but for MJO termination events. The composite values for a
960 termination event are marked with a circumscribed X for each phase. The composite history
961 before (12 days) and after (3 days) the termination event (i.e., last day before the combined
962 amplitude decays below unity) are shown in different colors for each phase.
963
964 **Figure 14.** Longitude-lag composites of the 20-100 day filtered anomalous (a)-(b) convective
965 heating ($\overline{H}a$), (d)-(e) moisture variable (q), and (g)-(h) zonal wind (u) from the model simulation
966 using the truncated, observed SSTs (Case-SST8N) for RMM phase 6 continuing and terminal
967 MJO events. All data are taken along the equator and composited for approximately 340 years.
968 Differences between terminal and continuing MJO events are shown in panels (c), (f), and (i) for
969 $\overline{H}a$, q, and u, respectively. The stippling in the difference panels indicates the presence of a
970 statistically significant different local mean for the continuing and terminating events (see

971 *Stachnik et al.* [2015] for further details). The number of events used for each composite (*N*) is
972 listed in the top-right corner of each panel.
973
974 **Figure 15.** As in Figure 14, but for the (a)-(c) zonal convergence and (d)-(f) potential
975 temperature (θ). (g)-(i) As in (d)-(f), but for a shorter, single 34 year period of skeleton model
976 data.
977
978 **Figure 16.** Box-whisker diagrams showing the distribution of (a) zonal wind (*u*) and (b)
979 moisture variable (*q*) anomalies for RMM phase 6 continuing and terminating MJO events
980 averaged over the local domain (120-160°E) at day -10. The 25%, 50%, and 75% percentiles
981 comprise the box lines with whiskers indicating the minimum and maximum values for all
982 events. The blue circles and red triangles represent the local-domain average values for
983 individual continuing and terminating MJO events, respectively. The mean quantities for each
984 event type are overlaid with a black star. All data are taken along the equator and represent 34
985 years of simulated MJO events using the truncated, observed SSTs (Case-SST8N).
986

987 **Table 1**. Maximum correlation coefficient from all lags comparing the structure of the leading

988 two EOFs between the skeleton model and observed *Wheeler and Hendon* [2004] RMM index

	EOF Variable		
EOF	Univariate (u)	Multivariate (u)	Multivariate ($-\bar{H}a$)
		Case-WP	
EOF1	0.85	0.83	0.70
EOF2	0.74	0.72	0.68
		Case-SST8N	
EOF1	0.98	0.98	0.89
EOF2	0.93	0.94	0.80

989

990 **Table 2**. Number of MJO events and average event length from observations (1979-2012) [a] and
991 an equivalent 34 year period[b] from the stochastic skeleton model using different EOFs to
992 calculate the SMM index for the simulation using an idealized warm pool (Case-WP)

	Event type (#)				
EOFs	Primary	Continuing	Circum-navigating	Terminal	Event length (d)
Univariate (*u*)	89.3±4.3	309.2±23.4	21.2±3.1	89.3±4.3	39.5±1.6
Multivariate (Model)	91.4±3.9	341±22.9	23.5±3.0	91.4±3.9	39.9±1.4
Multivariate (WH04[c])	97.7±3.5	343.4±17.9	23.7±2.0	97.7±3.5	40.2±1.1
Observations	154	330	15	154	34.9

993

994 [a]The observed MJO event numbers are taken from *Stachnik et al.* [2015]

995 [b]The model statistics and uncertainty estimates are generated from 680 years of model data that
996 comprise 20 independent samples of 34 year simulation periods

997 [c]WH04 refers to the case in which the observed *Wheeler and Hendon* [2004] EOFs are used in
998 place of the model quantities to calculate the SMM index and corresponding identification of
999 MJO events

1000 **Table 3**. As in Table 2, but for the simulation using the truncated, observed SSTs (Case-SST8N)

	Event type (#)				
EOFs	Primary	Continuing	Circum-navigating	Terminal	Event length (d)
Univariate (*u*)	98.3±2.8	443.5±31.5	33.4±3.6	98.3±2.8	43.3±1.7
Multivariate (Model)	98.4±3.2	466.8±31.2	35.5±3.4	98.4±3.2	43.8±1.5
Multivariate (WH04)	97.7±3.6	477.9±33.2	36.6±3.5	97.7±3.6	44.2±1.6
Observations	154	330	15	154	34.9

1001

1002 **Table 4**. Number of MJO events and average event length from observations (1979-2012) and an
1003 equivalent 34 year period from the stochastic and deterministic skeleton model simulations using
1004 the idealized warm pool (Case-WP and Case-WPdet) and truncated, observed SSTs (Case-
1005 SST8N and Case-SST8Ndet) projected on the *Wheeler and Hendon* [2004] EOFs

	Event type (#)				
Dataset	Primary	Continuing	Circum-navigating	Terminal	Event length (d)
Case-WP	97.7±3.5	343.4±17.9	23.7±2.0	97.7±3.5	40.2±1.1
Case-SST8N	97.7±3.6	477.9±33.2	36.6±3.5	97.7±3.6	44.2±1.6
Case-WPdet	90.8±2.3	797.3±29.0	75.3±3.7	90.8±2.3	61.5±2.2
Case-SST8Ndet	87.4±1.9	1316.7±26.6	140.1±3.2	87.4±1.9	77.7±1.8
Observations	154	330	15	154	34.9

1006

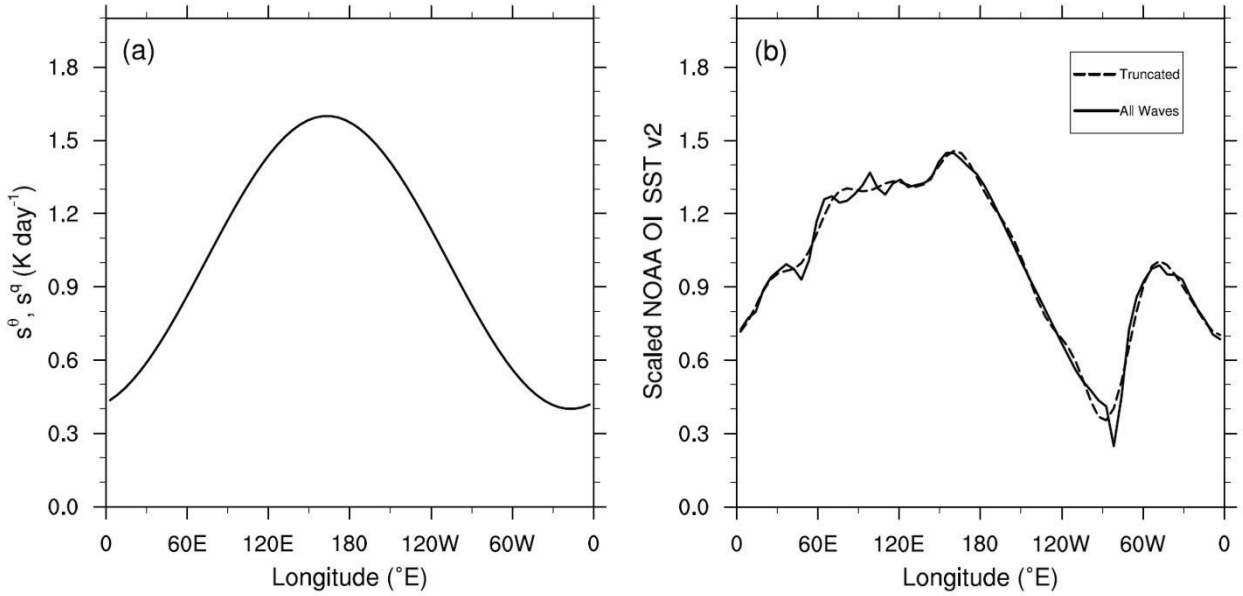

Figure 1. The shape of (a) the idealized warm pool (i.e., Case-WP) and (b) annual average (1971-2000) NOAA OI SSTs v2 used to force the skeleton model. The observed SSTs have been meridionally averaged from 10°S-10°N with a Poisson relaxation and interpolated over missing data (i.e., land). The solid line in (b) indicates the average SSTs from all waves downscaled to the model resolution of 625 km. The dashed profile in (b) has been smoothed to only retain the first eight Fourier modes (Case-SST8N).

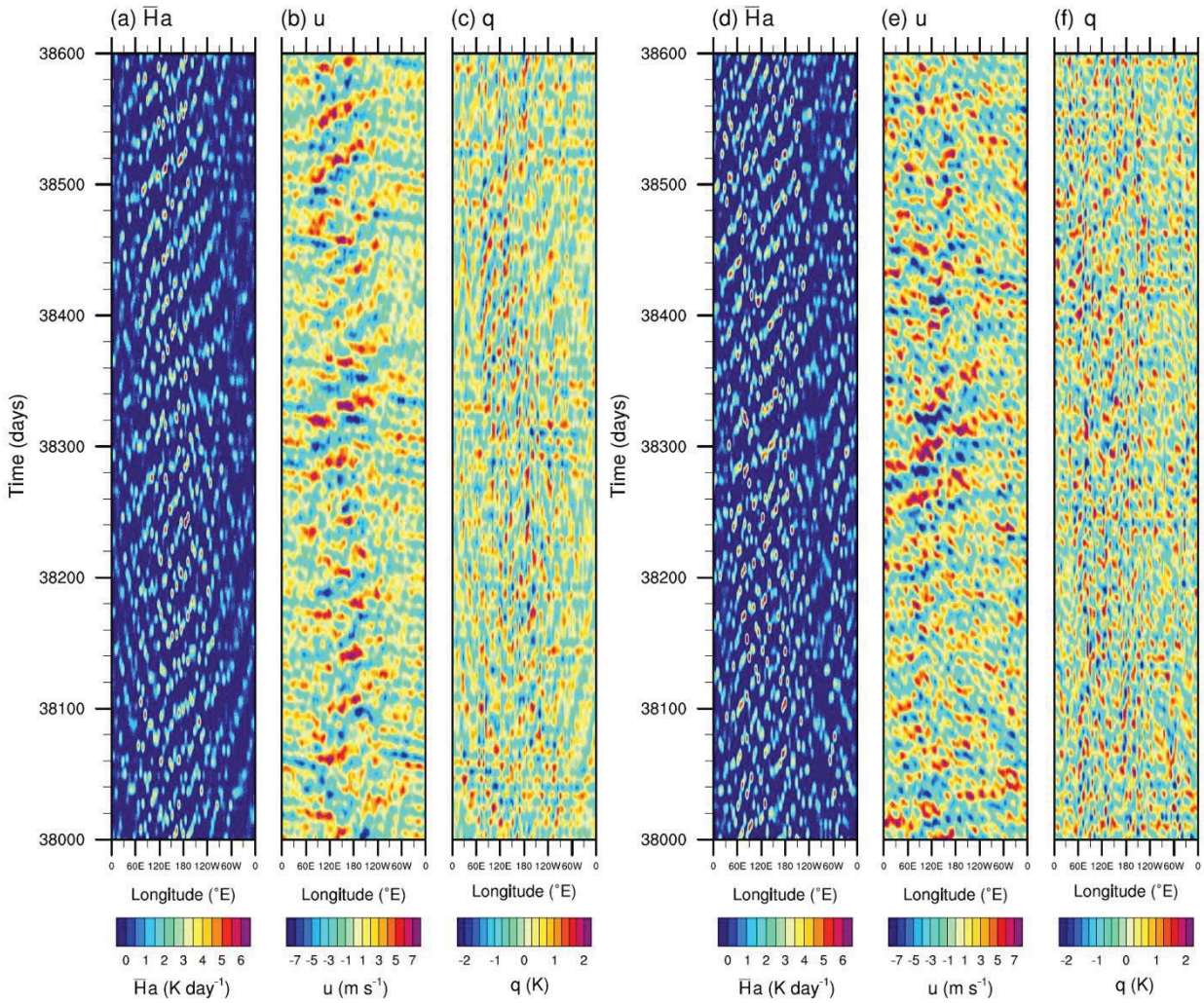

Figure 2. (a)-(c) Hovmöller diagrams of the anomalous 10-100 day filtered skeleton model variables for a 600 day period taken from the idealized warm pool simulation (Case-WP). All variables have daily resolution and are shown in dimensional units for the reconstructed (a) convective heating ($\overline{H}a$), (b) zonal wind (u), and (c) moisture (q) variables. (d)-(f) As in (a)-(c), but for the model simulation using the truncated, observed SSTs (Case-SST8N).

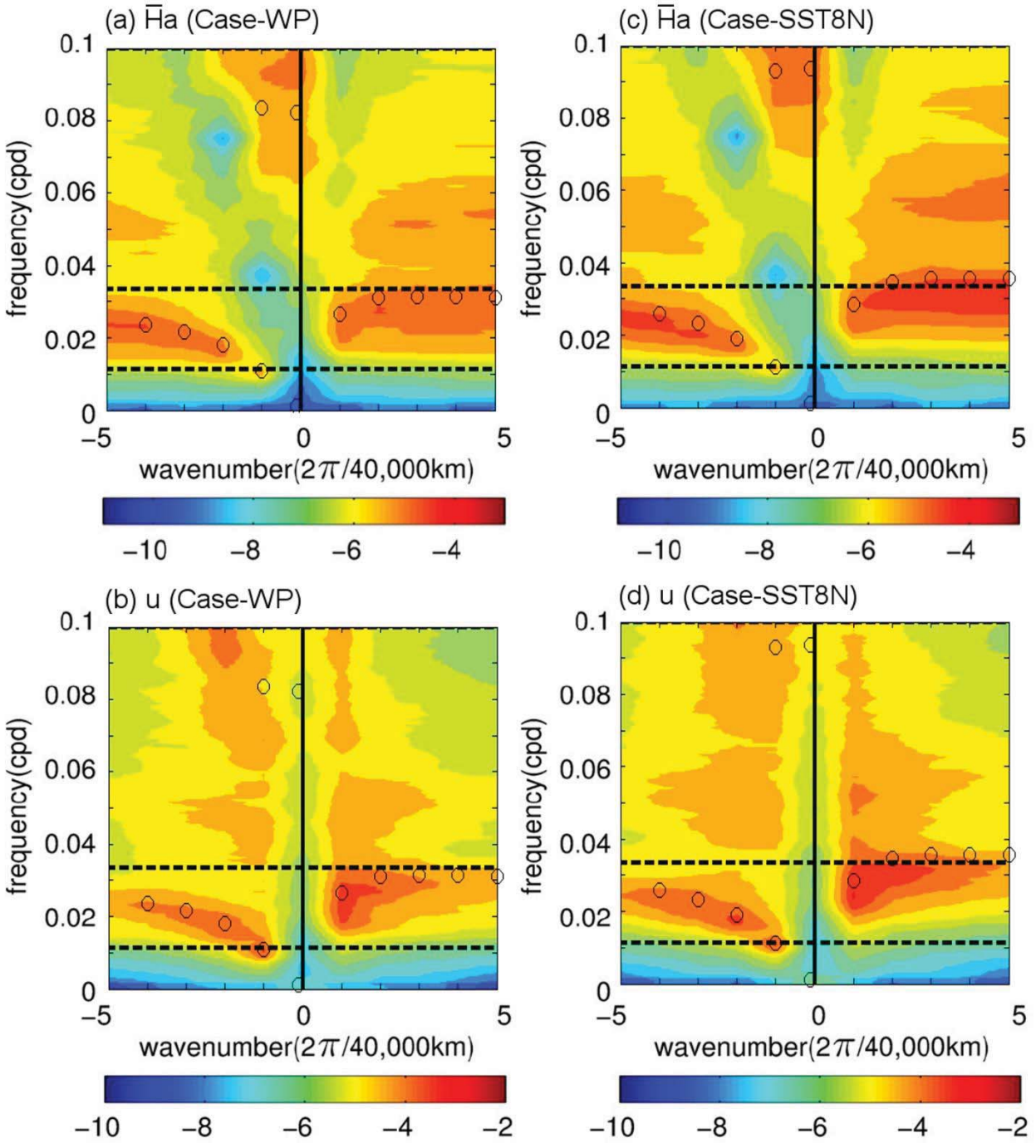

Figure 3. Zonal wavenumber-frequency power spectra of the (a) convective heating ($\overline{Ha}$, K day^{-1}) and (b) zonal wind (u, m s^{-1}) for the idealized warm pool case (Case-WP) from the skeleton model. Shading indicates the base-10 logarithm for the reconstructed and dimensional variables taken at the equator for approximately 34 years of model data. The black circles mark the dispersion curves from a separate stability analysis of the linear waves in the skeleton model in the Indian Ocean (67.5°E). The dashed, black lines indicate periods of 30 and 90 days. (c)-(d) As in (a)-(b), but for the model simulation using the truncated, observed SSTs (Case-SST8N).

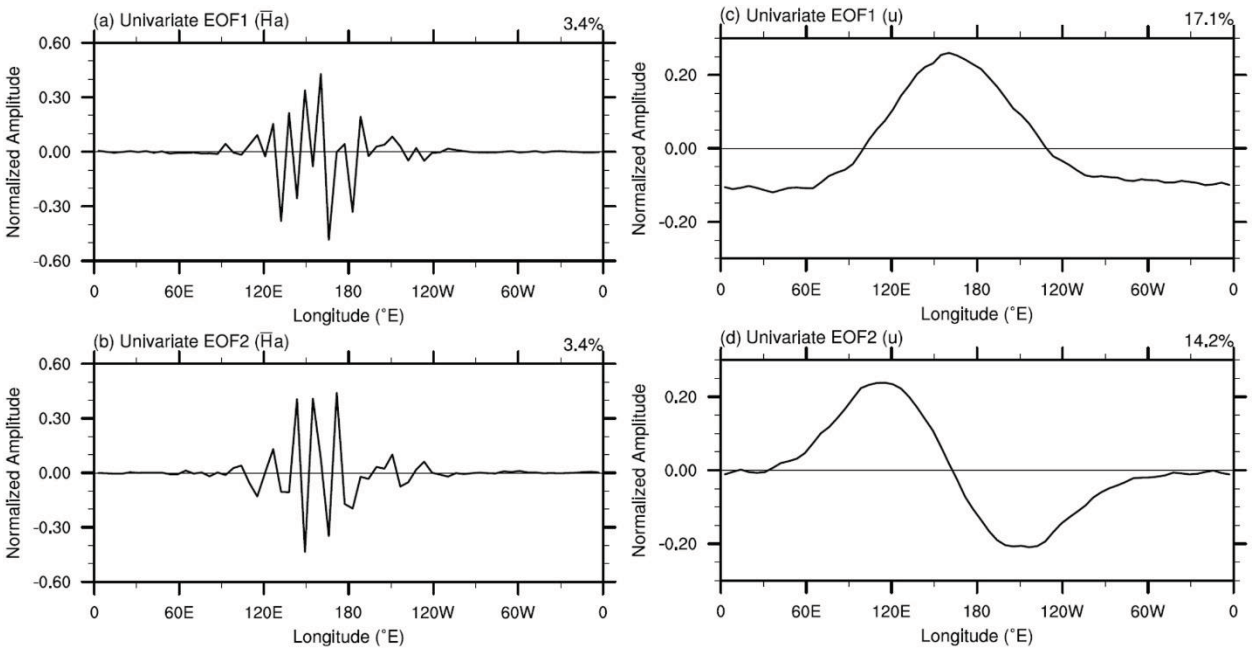

Figure 4. (a)-(b) The first two leading modes from a univariate EOF analysis of the 20-100 day filtered convective heating ($\overline{Ha}$) anomalies along the equator from approximately 340 years of the idealized warm pool simulation (Case-WP). (c)-(d) As in (a)-(b), but for a univariate EOF analysis of the zonal wind (u). The percent variance explained by each mode is shown in the upper-right of each panel.

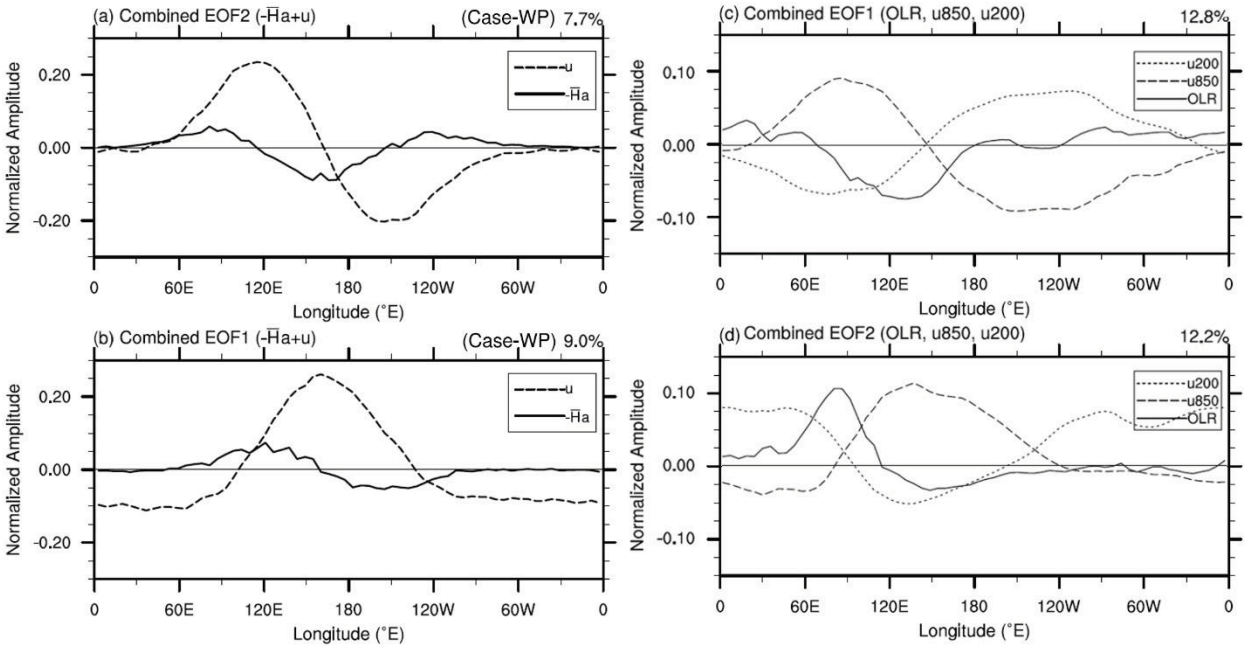

Figure 5. (a)-(b) The first two leading modes from a multivariate EOF analysis of the 20-100 day filtered convective heating ($-\overline{H}a$) and zonal wind (u) model anomalies along the equator from approximately 340 years of the idealized warm pool simulation (Case-WP). The order of EOF1 and EOF2 have been interchanged in addition to switching the sign of the convective heating term to better match the *Wheeler and Hendon* [2004] EOFs. (c)-(d) The first leading two modes from the observed multivariate analysis of *Wheeler and Hendon* [2004] showing the 15°S-15°N EOF structures of OLR and zonal wind at 850 hPa and 200 hPa (u850 and u200, respectively). The percent variance explained by each mode is shown in the upper-right of each panel.

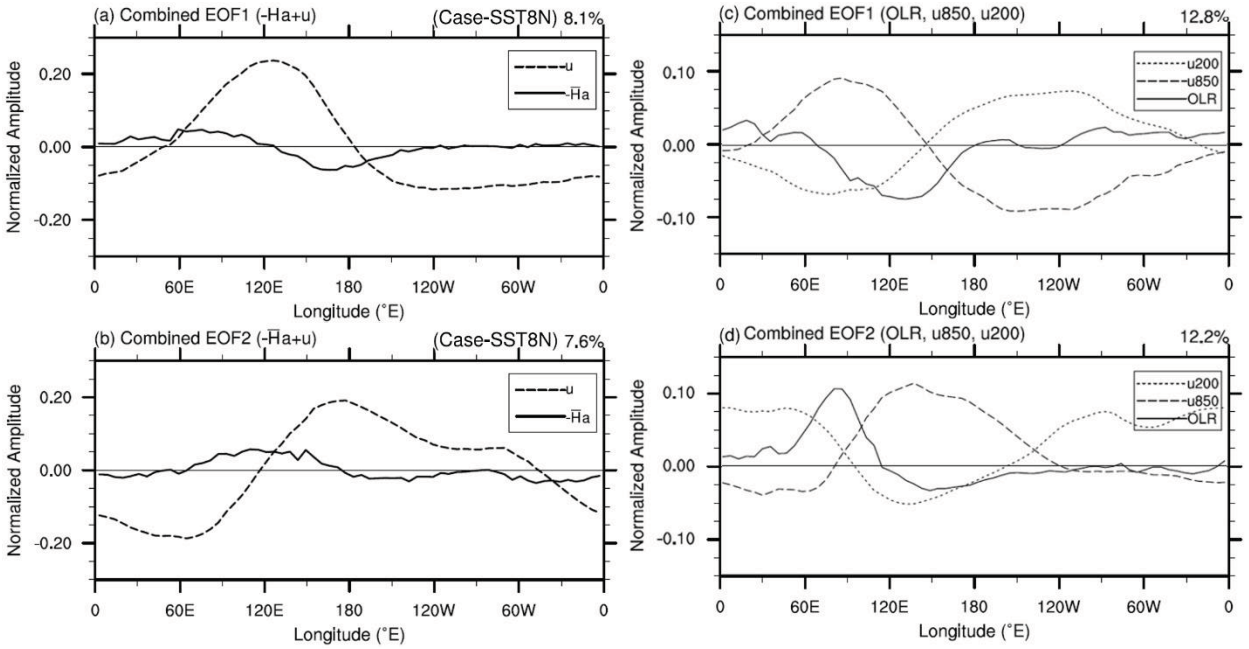

Figure 6. (a)-(b) As in Figure 5, but for the model simulation using the truncated, observed SSTs (Case-SST8N). Panels (c)-(d) are identical to Figure 5 to better facilitate comparison between the modeled and observed EOFs.

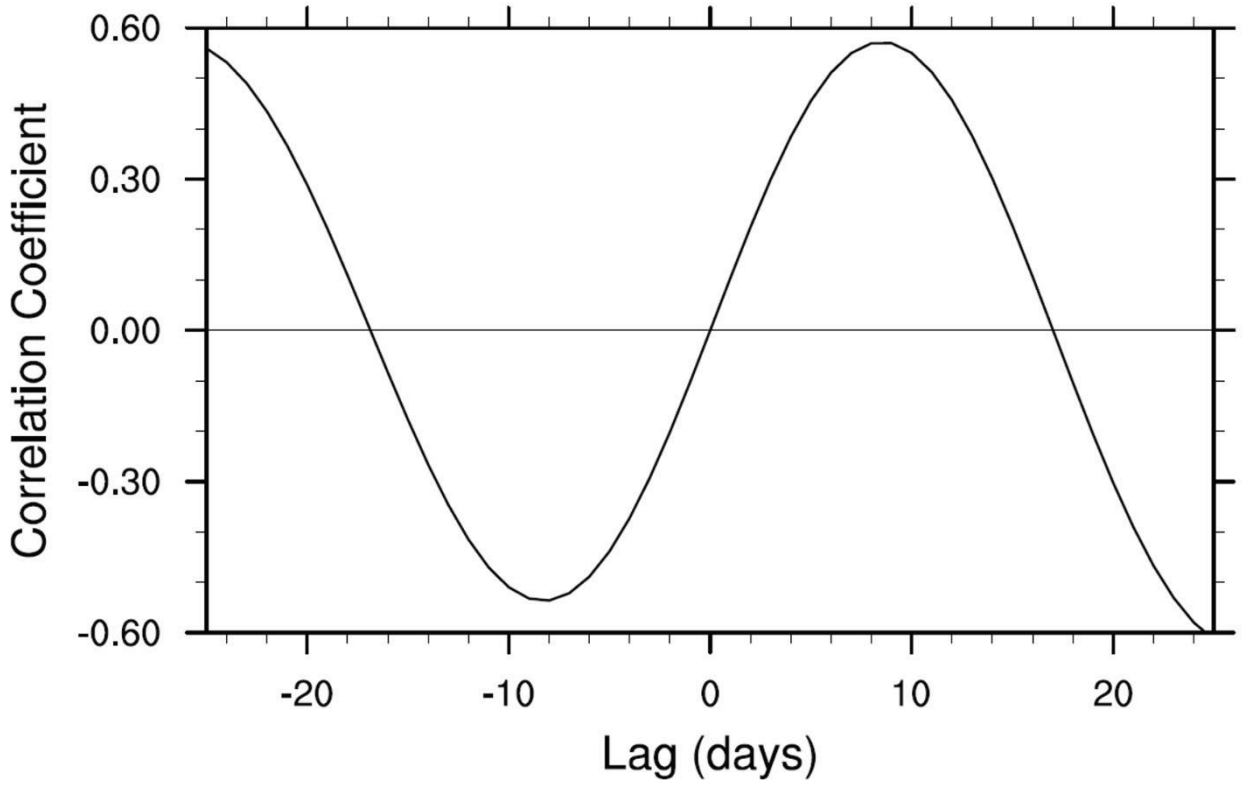

Figure 7. Lag correlations between the corresponding PC1 and PC2 from the multivariate EOF analysis of approximately 340 years of the model simulation using the truncated, observed SSTs (Case-SST8N).

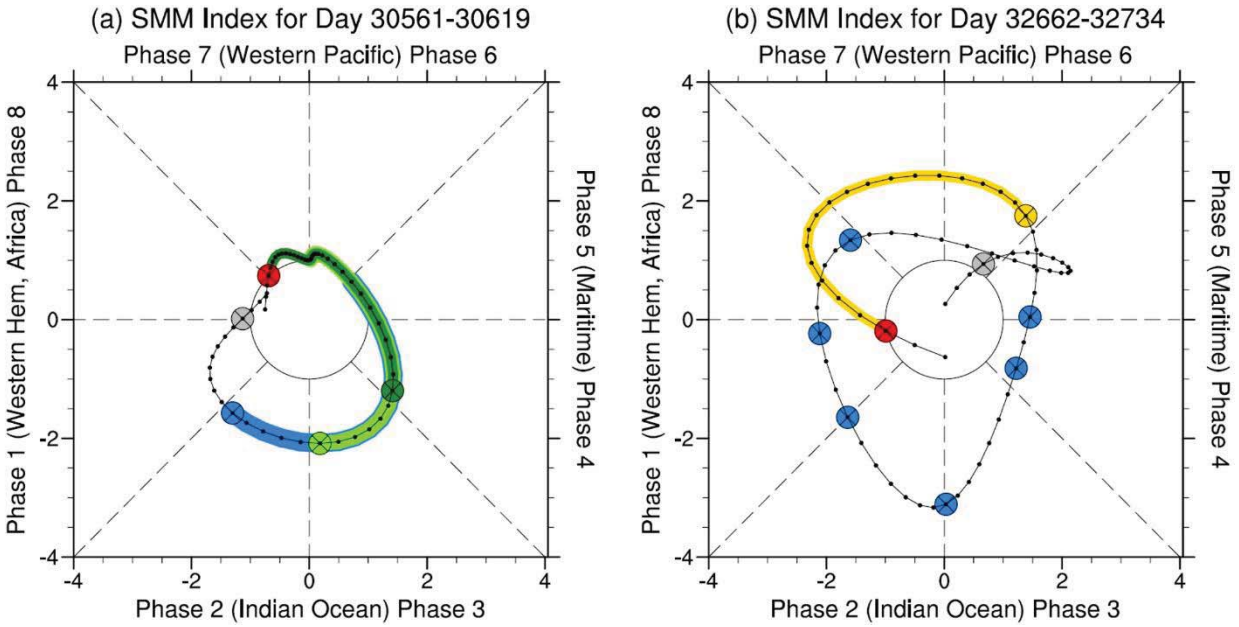

Figure 8. Examples of two MJO events using the skeleton multivariate MJO (SMM) index and the event criteria defined in *Stachnik et al.* [2015] for the model simulation using an idealized warm pool (Case-WP). The daily values of SMM1 and SMM2 (i.e., the principal components) are plotted as small dots for (a) day 30561-30619 and (b) day 32662-32734 in the 2-dimensional phase space obtained when projecting the model data onto the observed EOF patterns of *Wheeler and Hendon* [2004]. The initiation of a primary MJO event is shown in gray and indicated with a large, circumscribed X while the corresponding termination event is shown in red for each panel. Continuing MJO events are shown in blue and green in (a), with the subsequent history of the SMM index highlighted through the following four phases. The beginning of each continuing event are shown with a large, blue marker in (b) along with the start of a circumnavigating event and associated path highlighted in gold. Additional details and allowances provided by the identification algorithm are described in the text.

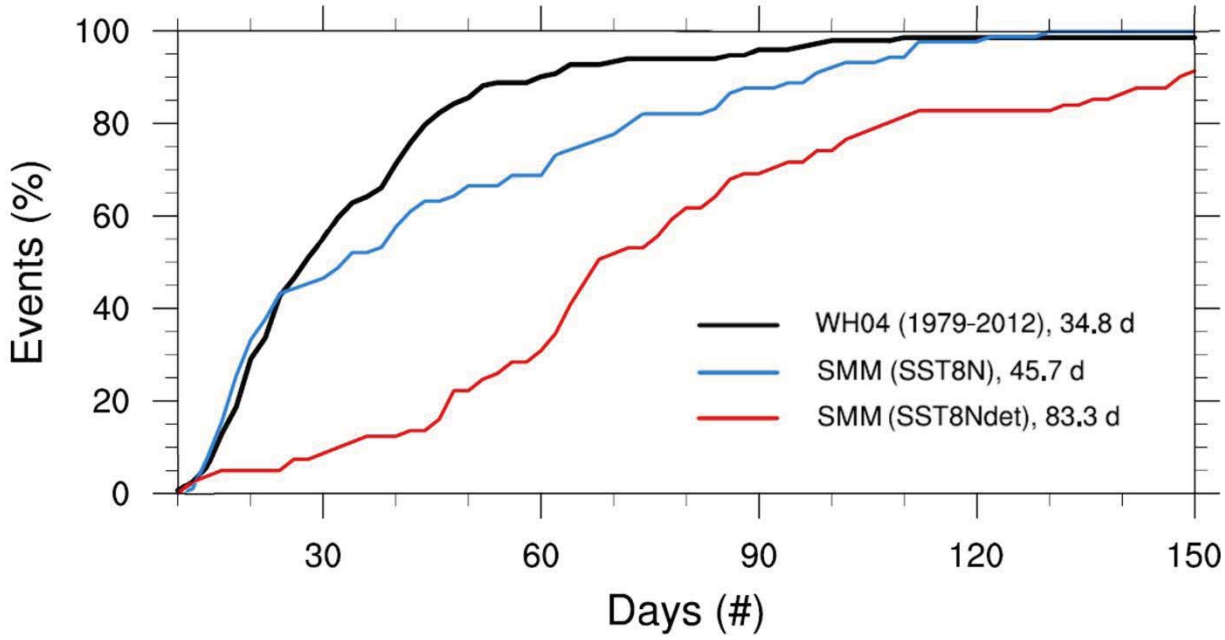

Figure 9. Cumulative probability distribution functions of the observed and modeled MJO event lengths from the stochastic model simulation using the truncated, observed SSTs (Case-SST8N), and a deterministic model simulation using the same SSTs (Case-SST8Ndet). The observed distribution is based on the historical *Wheeler and Hendon* [2004] RMM index from 1979-2012 and is represented by a thick, black line. The corresponding model event length distributions for similar 34 year periods are shown using thin, blue and red lines, respectively.

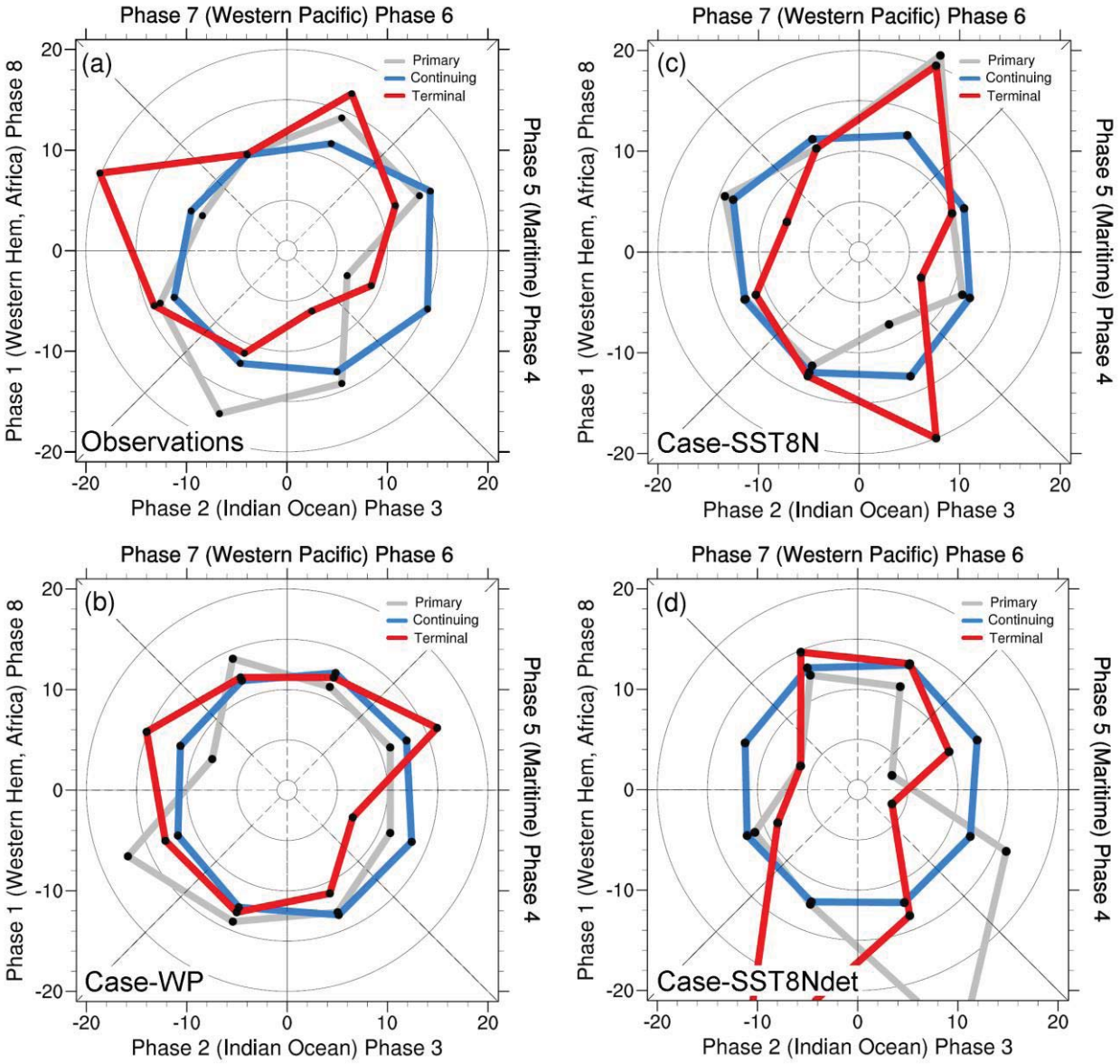

Figure 10. Radial-frequency diagrams showing the percent occurrence of MJO events as a function of RMM phase for (a) observations (1979-2012) and single 34 year periods from stochastic model simulations using (b) an idealized warm pool (Case-WP) and (c) the truncated, observed SSTs (Case-SST8N). (d) As in (c), but for the deterministic model simulation using the truncated and observed SSTs (Case-SST8Ndet). The black dots plotted at the center angle of each phase indicate the frequency of occurrence and are connected only for the ease of viewing primary, continuing, and terminal MJO events (gray, blue, and red lines, respectively). Range rings represent the 1%, 5%, 10%, 15%, and 20% frequencies of occurrence from the center to edge of the diagram, respectively.

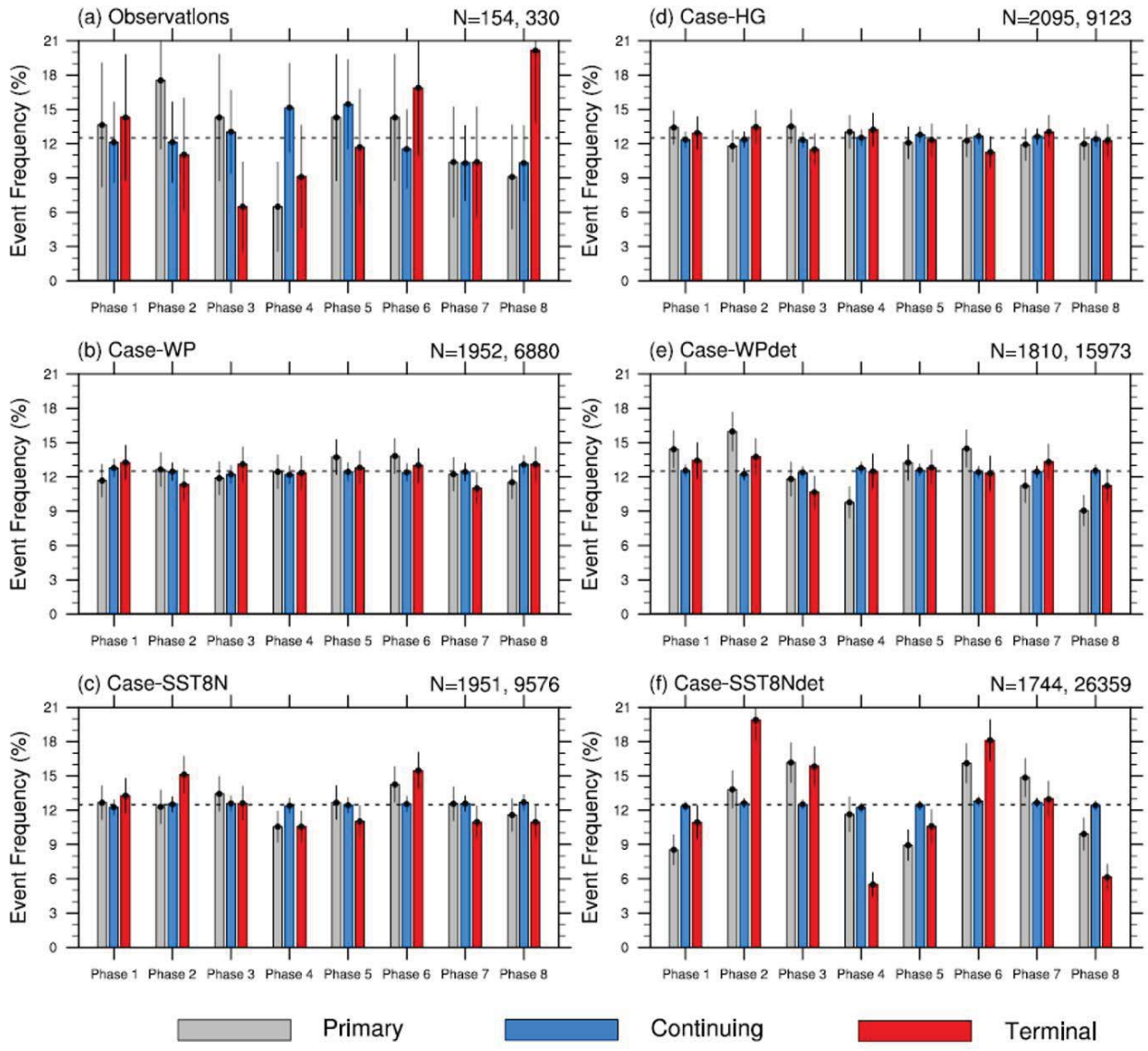

Figure 11. The mean frequency and uncertainty estimates of primary (gray), continuing (blue), and terminal (red) MJO events for each RMM phase in (a) observations and (b)-(f) approximately 680 years of model data. Simulations using an idealized warm pool and the truncated, observed SSTs (Case-WP and Case-SST8N, respectively) are shown in panels (b)-(c) with a special simulation using a homogeneous background state (Case-HG) in (d). Results from a deterministic version of the skeleton model using the idealized warm pool (Case-WPdet) and truncated, observed SSTs (Case-SST8Ndet) are shown in (e)-(f). The dashed line indicates the 12.5% frequency and represents the equal likelihood of an MJO event occurring in any phase. Error bars indicate the 95% uncertainty estimates and are calculated from a binomial proportion confidence interval (see text for details). The total number of primary/terminal and continuing events are indicated in the top right of each panel. All model simulations use the observed *Wheeler and Hendon* [2004] EOFs to calculate the principal components and corresponding MJO events with the exception of the homogeneous background case, which uses the multivariate EOFs obtained directly from the model data.

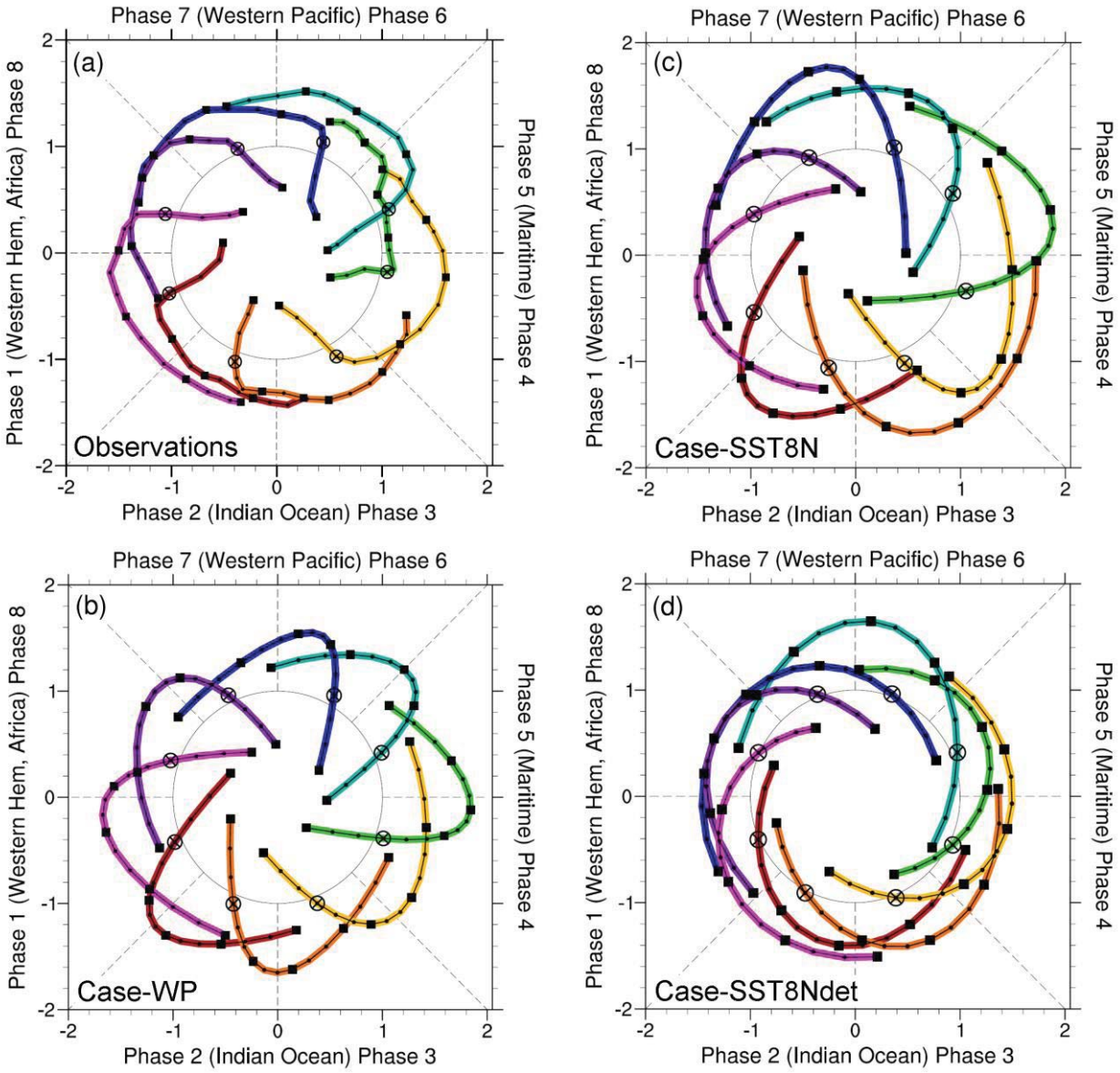

Figure 12. Initiation composites of the RMM1-RMM2 paths for (a) observations (1979-2012) and SMM1-SMM2 for an equivalent 34 year period from the stochastic model simulations using (b) an idealized warm pool (Case-WP) and (c) the truncated, observed SSTs (Case-SST8N). (d) As in (c), but for the deterministic model simulation using the truncated and observed SSTs (Case-SST8Ndet). The composite values for a primary event are marked with a circumscribed X for each phase. The composite history before (3 days) and after (12 days) the initiation event (i.e., first day after the combined amplitude grows above unity) are shown in different colors for each phase. The composite daily RMM and SMM values are plotted using small dots, while closed squares appear every three days for reference.

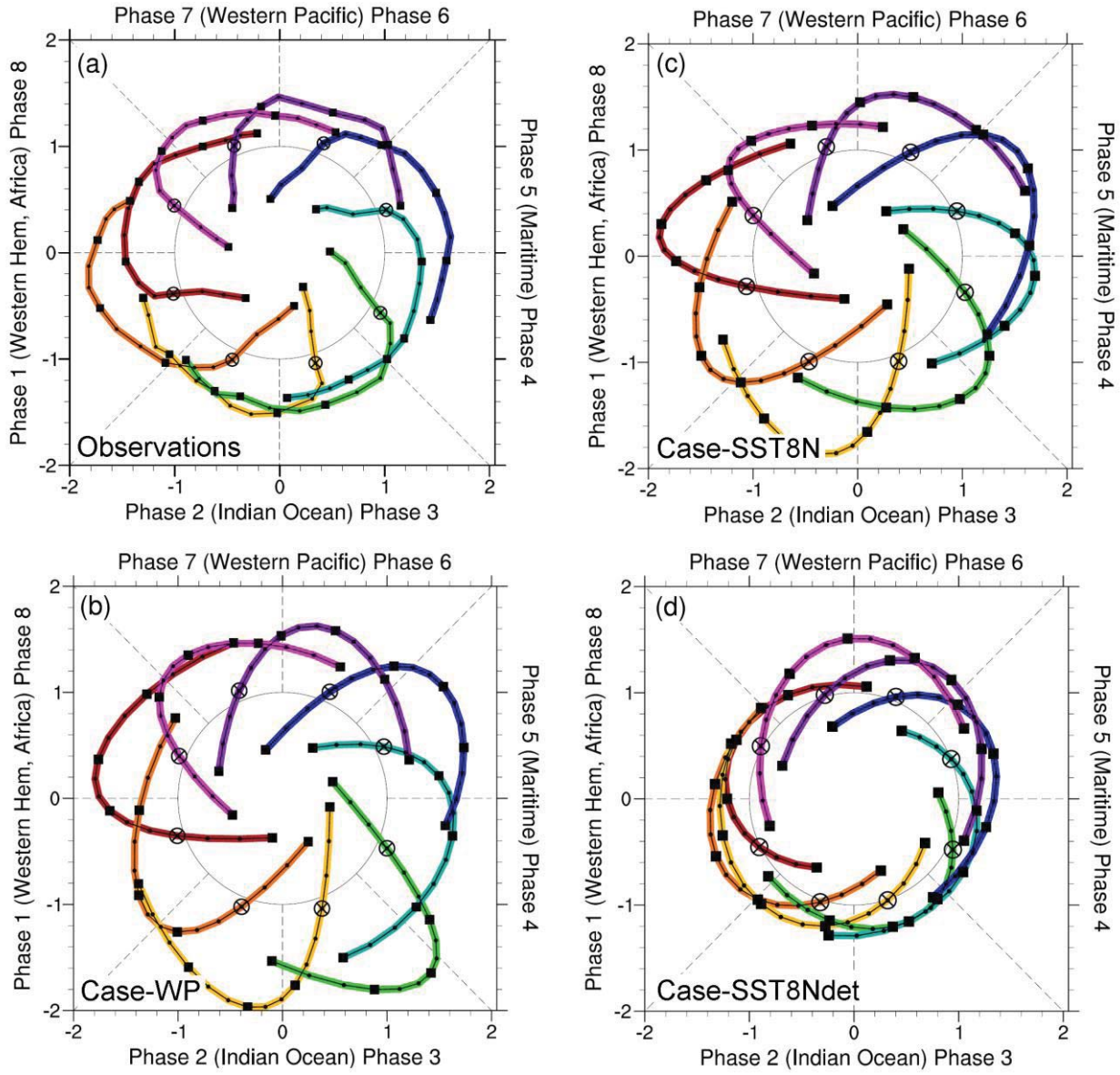

Figure 13. As in Figure 12, but for MJO termination events. The composite values for a termination event are marked with a circumscribed X for each phase. The composite history before (12 days) and after (3 days) the termination event (i.e., last day before the combined amplitude decays below unity) are shown in different colors for each phase.

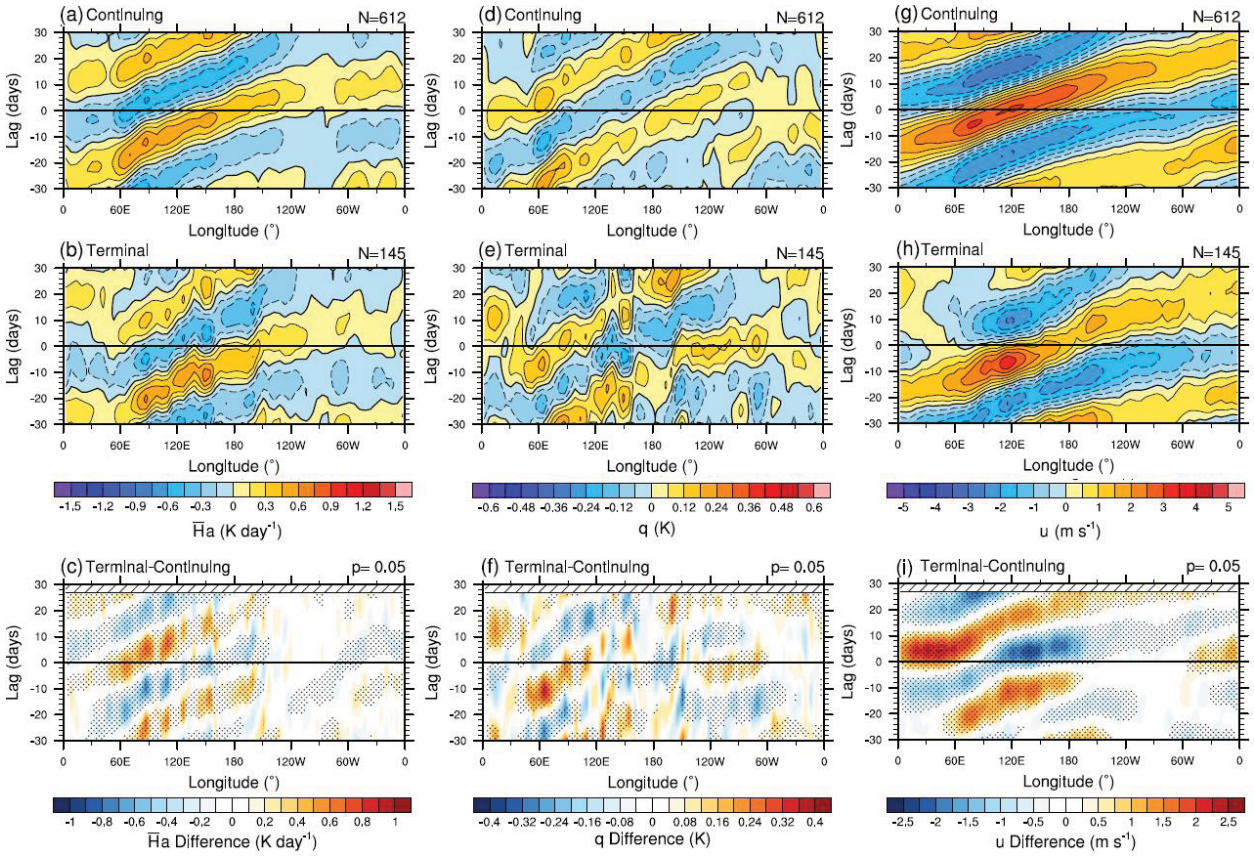

Figure 14. Longitude-lag composites of the 20-100 day filtered anomalous (a)-(b) convective heating ($\overline{H}a$), (d)-(e) moisture variable (q), and (g)-(h) zonal wind (u) from the model simulation using the truncated, observed SSTs (Case-SST8N) for RMM phase 6 continuing and terminal MJO events. All data are taken along the equator and composited for approximately 340 years. Differences between terminal and continuing MJO events are shown in panels (c), (f), and (i) for $\overline{H}a$, q, and u, respectively. The stippling in the difference panels indicates the presence of a statistically significant different local mean for the continuing and terminating events (see *Stachnik et al.* [2015] for further details). The number of events used for each composite (N) is listed in the top-right corner of each panel.

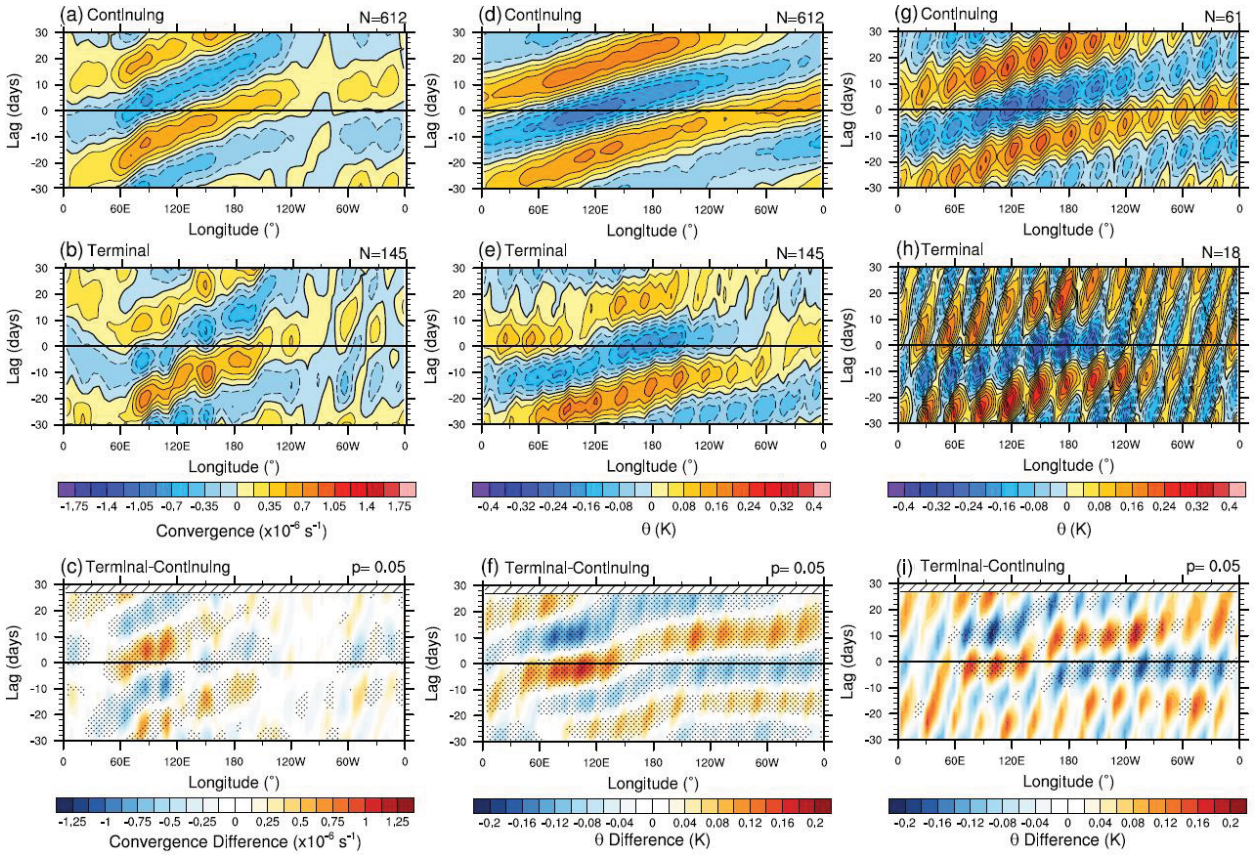

Figure 15. As in Figure 14, but for the (a)-(c) zonal convergence and (d)-(f) potential temperature (θ). (g)-(i) As in (d)-(f), but for a shorter, single 34 year period of skeleton model data.

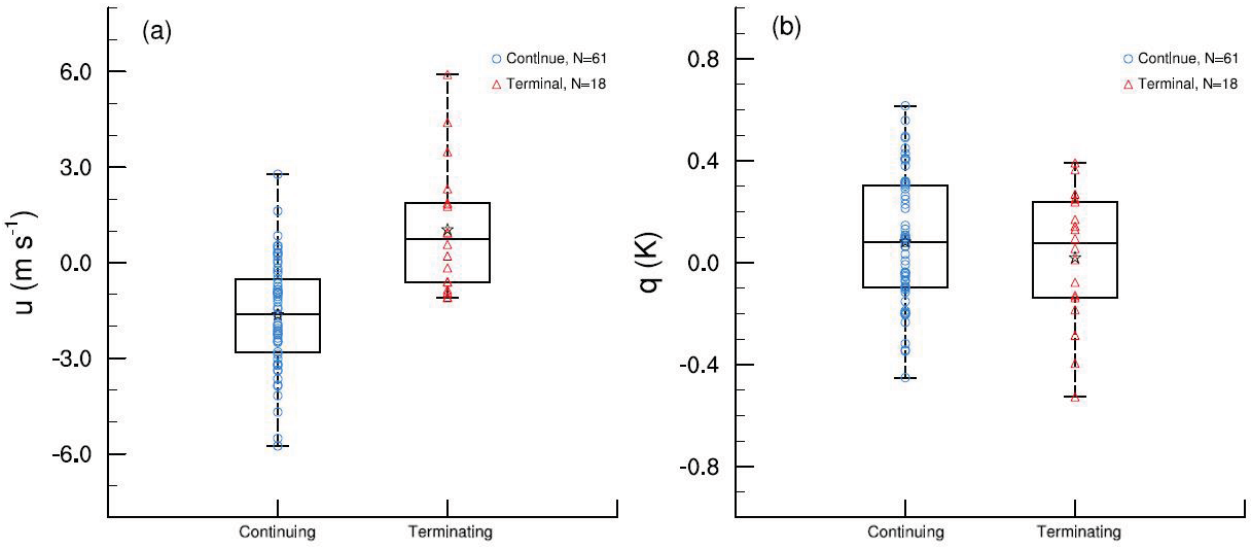

Figure 16. Box-whisker diagrams showing the distribution of (a) zonal wind (u) and (b) moisture variable (q) anomalies for RMM phase 6 continuing and terminating MJO events averaged over the local domain (120-160°E) at day -10. The 25%, 50%, and 75% percentiles comprise the box lines with whiskers indicating the minimum and maximum values for all events. The blue circles and red triangles represent the local-domain average values for individual continuing and terminating MJO events, respectively. The mean quantities for each event type are overlaid with a black star. All data are taken along the equator and represent 34 years of simulated MJO events using the truncated, observed SSTs (Case-SST8N).